

University of Memphis

University of Memphis Digital Commons

Electronic Theses and Dissertations

4-15-2012

A Study of Crustal and Upper Mantle Structure for the Eastern Tennessee Seismic Zone using P-wave Transfer Functions

Jordan H. Graw

Follow this and additional works at: <https://digitalcommons.memphis.edu/etd>

Recommended Citation

Graw, Jordan H., "A Study of Crustal and Upper Mantle Structure for the Eastern Tennessee Seismic Zone using P-wave Transfer Functions" (2012). *Electronic Theses and Dissertations*. 442.
<https://digitalcommons.memphis.edu/etd/442>

This Thesis is brought to you for free and open access by University of Memphis Digital Commons. It has been accepted for inclusion in Electronic Theses and Dissertations by an authorized administrator of University of Memphis Digital Commons. For more information, please contact khggerty@memphis.edu.

A STUDY OF CRUSTAL AND UPPER MANTLE STRUCTURE FOR THE
EASTERN TENNESSEE SEISMIC ZONE USING P-WAVE TRANSFER
FUNCTIONS

by

Jordan Hunter Graw

A Thesis

Submitted in Partial Fulfillment of the

Requirements for the Degree of

Master of Science

Major: Earth Sciences

The University of Memphis

May 2012

Copyright © 2012 Jordan Hunter Graw
All rights reserved

ACKNOWLEDGEMENTS

I would first and foremost like to thank everyone at the Center for Earthquake Research and Information for giving me the opportunity to learn and work with them. I feel very proud that Dr. Christine Powell noticed an interest I had and presented me with the opportunity to perform research in that area. I am grateful to Dr. Charles Langston for all of his unwavering help, be it obnoxious questions from me, or areas where I struggled, throughout the timeline of this project. Finding technical information on equipment (i.e. installation dates, removal dates, updates, calibrations, and instrument types) was simple thanks to the help of Dr. Mitch Withers and Jim Bollwerk. The faculty and staff at CERI have been the best to me, and I will never forget it.

To my closest friends at CERI, Lauren Kendall, John Meredith, Blaine Bockholt, and Sara Kelemencky, the time could not have flown by faster without you. It's always gratifying when you can count on others and they can count on you. The late nights studying, cramming, and getting projects put together is always a joy when there is friendly insight and criticism that is being added to each project.

I also thank my family for their support throughout my time working in Memphis. My parents, John and Cheryl Graw, have always supported every decision I have ever made to the fullest.

Finally, none of this would be possible without the support of my wife, Katelyn. Through late nights at CERI, to complaining at home, you never once suggested I give up. You are the reason I keep going, and I'll always love you for it.

“Insanity is doing the same thing, over and over again, but expecting different results.” – Albert Einstein

ABSTRACT

Graw, Jordan Hunter. M.S. The University of Memphis. May 2012. A study of crustal and upper mantle structure for the Eastern Tennessee Seismic Zone using P-wave transfer functions. Major Professor: Christine A. Powell, Ph.D.

We develop crust and mantle models of the Eastern Tennessee Seismic Zone (ETSZ) using imaging and inversion of the radial component P-wave transfer functions for stations in the Center for Earthquake Research and Information's (CERI) eastern Tennessee seismic network. We find complex structure in the upper 10 km in addition to an upper mantle high velocity zone with V_p values from ~ 8.2 - 8.56 km/s. This high velocity zone most likely extends from the west into the ETSZ and may be preserved mantle structure from the Granite Rhyolite province. Moho in the area is mostly gradational. However, velocity discontinuities can be seen at places indicating a fairly stable Moho depth of ~ 45 - 50 km. We suggest that the NY-AL lineament represents a major deep crustal to upper mantle feature.

TABLE OF CONTENTS

	PAGE
List of Tables	vi
List of Figures	viii
Introduction	1
Tectonic Setting	3
Data and Data Processing	14
Transfer Functions	16
Transfer Function P-wave Equalization	17
Waveform Inversion	27
Synthetic Inversion	34
Results	36
Comparison Against a Broadband Seismometer	43
Discussion	47
Conclusions	51
References	52
Appendices	
A. List of Events for this Study	55
B. Inversion Results for each Station	58

LIST OF TABLES

TABLE	PAGE
1: Table showing the number of waveforms within each stations' vertical, radial, and tangential transfer function stack.	21
2: Values for initial model ET1D. Velocities are in km/s, density in g/cc, and thickness is in km. (from Vlahovic <i>et al.</i> , 1998).	28
3: Values for modified ET1D that is used in our inversions. Velocities are in km/s, density in g/cc, and thickness is in km.	29
4: Table showing the list of events used in this study. Velocities are in km/s, density in g/cc, and thickness is in km.	56
5: Inversion values corresponding to results from Figure 12 for station BCRT. Velocities are in km/s, density in g/cc, and thickness is in km.	59
6: Inversion values corresponding to results from Figure 12 for station CCRT. Velocities are in km/s, density in g/cc, and thickness is in km.	60
7: Inversion values corresponding to results from Figure 12 for station CMGA. Velocities are in km/s, density in g/cc, and thickness is in km.	61
8: Inversion values corresponding to results from Figure 12 for station CPCT. Velocities are in km/s, density in g/cc, and thickness is in km.	62
9: Inversion values corresponding to results from Figure 12 for station DYTN. Velocities are in km/s, density in g/cc, and thickness is in km.	63
10: Inversion values corresponding to results from Figure 12 for station ETT. Velocities are in km/s, density in g/cc, and thickness is in km.	64
11: Inversion values corresponding to results from Figure 12 for station GMG. Velocities are in km/s, density in g/cc, and thickness is in km.	65

12: Inversion values corresponding to results from Figure 12 for station GRBT. Velocities are in km/s, density in g/cc, and thickness is in km.	66
13: Inversion values corresponding to results from Figure 12 for station RCGA. Velocities are in km/s, density in g/cc, and thickness is in km.	67
14: Inversion values corresponding to results from Figure 12 for station SMNC. Velocities are in km/s, density in g/cc, and thickness is in km.	68
15: Inversion values corresponding to results from Figure 12 for station SWET. Velocities are in km/s, density in g/cc, and thickness is in km.	69
16: Inversion values corresponding to results from Figure 12 for station TVNC. Velocities are in km/s, density in g/cc, and thickness is in km.	70
17: Inversion values corresponding to results from Figure 12 for station TZTN. Velocities are in km/s, density in g/cc, and thickness is in km.	71

LIST OF FIGURES

FIGURE	PAGE
1: Tectonics of the eastern US throughout two Wilson cycles. a) Assembly of Rodinia. b) Breakup of Rodinia and opening of apetus Ocean. c) Assembly of Pangaea. d) Breakup of Pangaea and opening of Atlantic Ocean. (modified from Thomas, 2006).	5
2: Structure cross section inferred from the COCORP line through the southern Appalachians. Green colors represent the Carolina Terrane. Pink represents the Piedmont Province. Blue epresents the Blue Ridge Province. Light Blue represents the Valley and Ridge Province. The ETSZ, shown by the X, is located mainly below the Valley and Ridge Province. (modified from Cook and Vasudevan, 2006).	7
3: Magnetic and gravity anomalies within the ETSZ. The NY-AL lineament is labeled in each map. a) Magnetic anomaly map. Notice the high magnetic signature west of the lineament and the low magnetic signature east of the lineament. b) Bouguer gravity anomaly map. The gravity highs and lows correlated with the magnetic highs and lows in some places. However, in some instances, the potential ields are anticorrelated. An example is the gravity low associated with the NY-AL lineament magnetic high. Data obtained from GeoNet Gravity and Magnetic Dataset Repository from the University of Texas at El Paso (http://irpsrvgis00.utep.edu/repositorywebsite).	10
4: Map depicting locations of 8 seismic reflection lines from COCORP and the Great Lakes International Multidisciplinary Program on Crustal Evolution (GLIMPCE): TN-3, TN-4, IN-1, OH-1, OH-2, NY-7, and NY-8 from COCORP. GFTZ and the Amish Anomaly are appropriately labeled as the SW-NE trending lineaments. (from Culotta <i>et al.</i> , 1990).	11
5: Map depicting local seismicity within the ETSZ. The NY-AL and Clingman lineaments are labeled above. Notice seismicity confined primarily to the SE side of the NY-AL lineament. 921 events from CERI <i>seisnet</i> database, spanning 1984-2009.	11
6: P-wave (left) and S-wave (right) velocity anomalies for the ETSZ. Slices in 4 km intervals. Red indicates low velocities and blue indicates high velocities. Notice at depth how P-wave velocities begin to lose resolution, but S-wave velocities intensify. (modified from Powell, 2012).	12

7: Map showing the outline of our study area. Study area is within the red box.	13
8: ETSZ network station map. Red stations have S-13 short-period seismometers. Blue stations broadband seismometers. The broadband station TZTN is maintained by IRIS. Stations' instruments are described previously.	15
9: Map depicting events used in this study.	15
10: Transfer function ray diagram. Above shows the rays as they transmit through a boundary. Blue lines represent S waves. Orange lines represent P waves. Below shows the phases present in a transfer function. The phases in the transfer function can be seen in the diagram above it for any clarification. The Ps phase is the direct converted phase from a given boundary (namely the Moho), while the other phases are the multiples from that given boundary.	16
11: Radial and tangential component transfer function comparison. Both radial and tangential waveforms are stacks. Black line represents the radial component. Red line represents the tangential component. These stations yield acceptable inversion results.	22
12: Radial and tangential component transfer function comparison. Both radial and tangential waveforms are stacks. Black line represents the radial component. Red line represents the tangential component. These stations yield inconsistent inversion results and bad waveform fits.	25
13: Initial velocity model, ET1D. Values in Table 2. (from Vlahovic <i>et al.</i> , 1998).	28
14: Initial model used in inversions. Values in Table 3. Model was created by the forward modeling technique described earlier.	29
15: Results from a synthetic inversion. a) V_p profiles for the initial model (black), the final model (red), and ET1D (blue). b) Waveforms associated with the inversion. Black line is the synthetic created using ET1D. Red line is the final waveform from the inversion. Dashed line is the synthetic seismogram from the initial model.	35
16: Waveform inversion results from stations BCRT, CCRT, CMGA, CPCT, DYTN, and ETT. Waveforms inverted are stacked waveforms. Black line represents the radial receiver function data. Red lines represent the inversion results with varying smoothing constraints.	37

16 cont.:	Waveform inversion results from stations GMG, GRBT, RCGA, SMNC, SWET, and TVNC. Waveforms inverted are stacked waveforms. Black line represents the radial receiver function data. Red lines represent the inversion results with varying smoothing constraints.	38
16 cont.:	Waveform inversion result from station TZTN. Waveform is a stacked waveform. Black line represents the radial receiver function data. Red lines represent the inversion results with varying smoothing constraints.	39
17:	P-wave velocity profiles for stations BCRT, CCRT, CMGA, CPCT, DYTN, and ETT. Each inversion is the result of using a different smoothing parameter. Range of smoothing parameters is labeled above each profile and increases 0.1 for each inversion. Moho and any gradational Moho is labeled. Red circles represent the 60 km depth high velocity zone. Blue circles represent the 65 km depth high velocity zone.	40
17 cont.:	P-wave velocity profiles for stations GMG, GRBT, RCGA, SMNC, SWET, and TVNC. Each inversion is the result of using a different smoothing parameter. Range of smoothing parameters is labeled above each profile and increases 0.1 for each inversion. Moho and any gradational Moho is labeled. Red circles represent the 60 km depth high velocity zone. Blue circles represent the 65 km depth high velocity zone.	41
17 cont.:	P-wave velocity profile for station TZTN. Each inversion is the result of using a different smoothing parameter. Range of smoothing parameters is labeled above the profile and increases 0.1 for each inversion. Moho and any gradational Moho is labeled. Red circles represent the 60 km depth high velocity zone. Blue circles represent the 65 km depth high velocity zone.	42
18:	Comparison between the broadband and short-period methodologies at station CPCT. Event from 02/16/2008 in Potosi, Bolivia. a) Broadband radial component transfer function. b) Short-period radial component transfer function. c) Broadband inversion results (P-wave profile). d) Short-period inversion results (P-wave profile).	44
18 cont.:	Results from station SWET. e) Broadband radial component transfer function. f) Short-period radial component transfer function. g) Broadband inversion results (P-wave profile). h) Short-period inversion results (P-wave profile).	45

18 cont.: Results from station TZTN. i) Broadband radial component transfer function. j) Short-period radial component transfer function. k) Broadband inversion results (P-wave profile). l) Short-period inversion results (P-wave profile). 46

19: Maps depicting some of the various boundaries found in the inversion results. a) Map where Moho discontinuities can be seen. Black is a station where the Moho can be clearly seen on the velocity profile. The Moho is generally around 46-48 km depth within the ETSZ. Gray is a station where the Moho is somewhat noticeable. Clear circles are stations where the Moho is gradational and does not show any sharp discontinuities. b) Locations where the 60-65 km upper mantle high velocity zone can be seen. Black is a 60 km depth high velocity zone, and gray is a 65 km depth high velocity zone. Notice the abrupt drop from 60 to 65 km across the NY-AL lineament. 50

INTRODUCTION

Distinct intraplate seismic zones are globally rare but two, the Eastern Tennessee Seismic Zone (ETSZ) and the New Madrid Seismic Zone (NMSZ), occur in the central United States. The driving mechanism(s) for intraplate seismic zones is unknown and is a subject of great debate. Most studies indicate that intraplate seismicity is associated with ancient rift zones (e.g. Johnston and Kanter, 1990), but this is probably not the case for the ETSZ. Our knowledge of basement features influencing the ETSZ is limited due to a lack of geophysical investigations in the area, inadequate seismograph coverage, low numbers of high magnitude local and regional earthquakes, and a lack of earthquakes that can be associated with a known subsurface feature (Powell *et al.*, 1994). A better understanding of basement subsurface features beneath the ETSZ may suggest a causative mechanism for the seismicity of the area.

Transfer functions can be used to study deep crustal and upper mantle structure and are somewhat different from receiver functions. The stacked source function used in the deconvolution process for transfer functions preserves both P-wave and S-wave conversions and multiples within the resultant radial component function. Receiver functions are created by using recording components from a single station and theoretically have only Ps-wave conversions within the receiver function. Transfer function studies allow us to image the subsurface by visually displaying Ps conversions at varying depths. Inverting these transfer function waveforms allow us to obtain new earth structure models in the form of velocities (both V_P and V_S) and densities for a number of layers. These results will give us insight into the crustal and upper mantle features

directly below any given seismic station and may make it possible to relate local seismicity to subsurface geologic features.

The purpose of this study is to infer prominent geologic subsurface features beneath the ETSZ. Because of data availability, we utilize short-period data that will provide comparable resolution within the crust and upper mantle as broadband data. Past studies have found interesting basement features just outside of our study area, and we anticipate finding equally important features in our study. Of course, determining Moho depth and its variation are among our main goals as that is what transfer functions image best. We know there is a large decollement in our area, and expect to detect that as well. Transfer functions can also image upper mantle features. Upper mantle and lower crustal features can put constraints on tectonics in the area. Knowledge of any new subsurface feature could be used to correlate the geology with the local seismicity and give new insight into the past tectonics of the eastern US.

TECTONIC SETTING

Basement rocks hosting the ETSZ lie within a zone of complicated terrane accretions mainly associated with the Grenville orogeny of the Proterozoic. The Grenville front is thought to lie just to the west of the ETSZ, although the exact location is unknown (Figure 1) (Keller *et al.*, 1982). Hopkins (1995) speculates that the Grenville front lies below the ETSZ, based upon reprocessed industry reflection lines. The Granite Rhyolite province and the Grenville terrane are the major basement rocks within the eastern US. The Granite Rhyolite province basement lies to the west of the Grenville front (Figure 1a). The opening of the Iapetus Ocean caused extension and faulting that cut across intra-Grenville suture zones (Figure 1b) (Thomas, 2006). These faults are preserved in the ancient Grenvillian basement but are probably not associated with the ETSZ. Rather, potential field data suggest that the ETSZ is associated with a major transpressive basement feature (Cullota *et al.*, 1990). Within the ETSZ the Grenvillian basement has been overridden by Appalachian-Ouachita orogenic rocks associated with the Alleghanian Orogeny (Figure 1c) (Thomas, 2006). Reprocessing of the Consortium for Continental Reflection Profiling (COCORP) reflection profiles of 1978-1980 shows that overlying rocks of the Valley and Ridge, Blue Ridge and Inner Piedmont provinces are separated from the autochthonous Grenvillian basement by a major horizontal detachment fault or decollement (Figure 2) (Cook and Vasudevan, 2006).

Just to the west of the ETSZ a possible Keweenawan-aged rift system may exist (Keller *et al.*, 1982; Owens *et al.*, 1987). This upper to mid crustal high-velocity feature is associated with large, positive gravity and magnetic anomalies and forms part of the postulated East Continent Gravity High (ECGH) shown in Figure 3b (Keller *et al.*, 1982).

Gravity and magnetic anomalies within the ETSZ are characterized by abrupt changes across an aeromagnetic feature known as the New York-Alabama (NY-AL) magnetic lineament. The NY-AL lineament is oriented NE-SW and runs from northern Alabama to New York (King and Zietz, 1978; Steltenpohl *et al.*, 2010). This lineament is characterized by a large contrast in magnetic and, to a lesser extent, gravity anomalies (Figure 3).

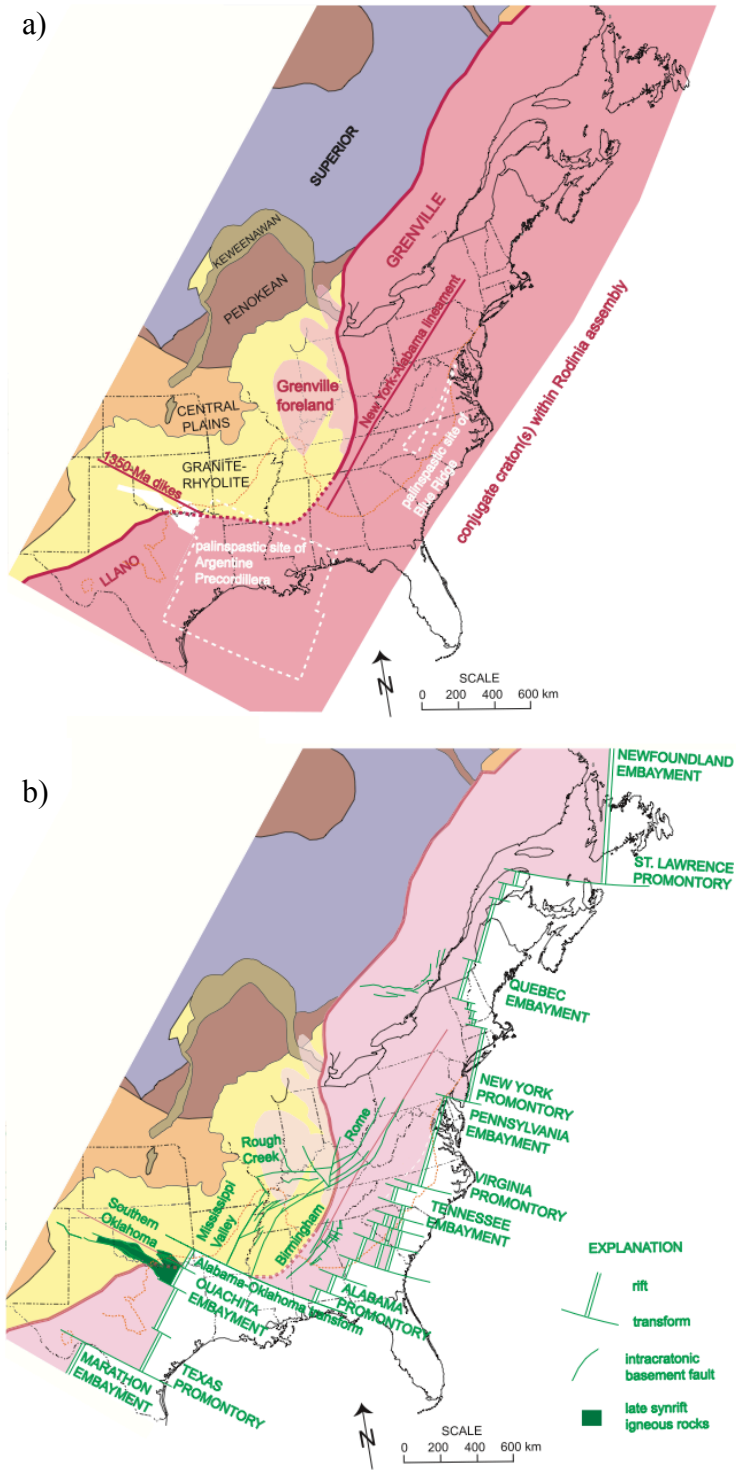


Figure 1: Tectonics of the eastern US throughout two Wilson cycles. a) Assembly of Rodinia. b) Breakup of Rodinia and opening of Iapetus Ocean. (modified from Thomas, 2006).

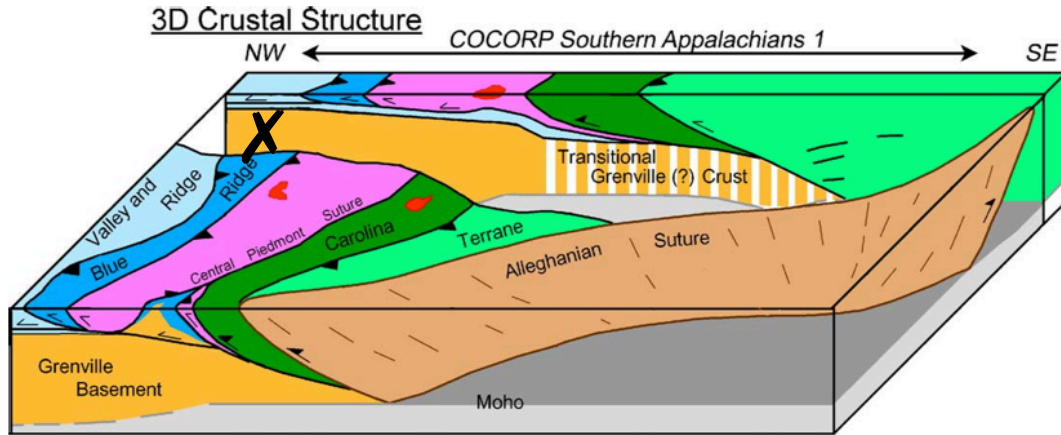


Figure 2: Structure cross section inferred from the COCORP line through the southern Appalachians. Green colors represent the Carolina Terrane. Pink represents the Piedmont Province. Blue represents the Blue Ridge Province. Light Blue represents the Valley and Ridge Province. The ETSZ, shown by the X, is located mainly below the Valley and Ridge Province. (modified from Cook and Vasudevan, 2006).

Magnetic highs are located to the west of the NY-AL lineament and lows are to the east.

In other areas outside of the ETSZ, the polarity changes, but the contrasts produce a steep gradient along most of the NY-AL lineament. Bouguer gravity anomalies are relatively higher to the east of the lineament and lower to the west. Some studies indicate that the NY-AL lineament is better described by the NE-SW trending Amish anomaly north of West Virginia (Figure 4) (Culotta *et al.*, 1990; Steltenpohl *et al.*, 2010). The two anomalies coincide towards their southern ends and are more or less the same anomaly.

The origin of the NY-AL lineament is enigmatic. One model is that it is an ancient sinistral strike-slip fault (Bartholomew and Hatcher, 2010). A contrasting viewpoint is that it is a dextral strike-slip fault (Steltenpohl *et al.*, 2010). Others suggest that the NY-AL/Amish lineation marks a major transpressional suture zone based upon basement features imaged in Ohio by COCORP (Culotta *et al.*, 1990) and extension of potential field trends into Canada. Shifts in isotopic signatures across the NY-AL

lineament suggest that the lineament is a remnant of a Mesoproterozoic suture between the Granite-Rhyolite and Grenvillian basements located in the subsurface (Fisher *et al.*, 2010).

Local seismicity within the ETSZ is confined primarily to the region between the NY-AL and the Clingman magnetic lineaments (Figure 5). Earthquakes within the region occur at depths of 5-26 km within the Grenville basement (Chapman *et al.*, 1997; Vlahovic *et al.*, 1998).

ETSZ seismicity follows the NY-AL lineament, even changing trend in northern Alabama, and most earthquakes occur southeast of the lineament (Figure 5). Focal mechanisms reveal that dextral NS trending or sinistral EW trending strike-slip faulting occurs throughout the ETSZ (Chapman *et al.*, 1997). Results from fault orientation studies show dominant fault strikes are compatible with fault orientations to be expected from the present-day stress field (Chapman *et al.*, 1997).

Previous work, utilizing various geophysical techniques, lays the foundation for this study. Reprocessed COCORP lines across the Carolina terrane, Piedmont, and Blue Ridge provinces reveal an autochthonous Grenvillian basement overridden by Appalachian thrust sheets along a major detachment fault (Figure 2) (Cook and Vasudevan, 2006). The thickness of overriding Appalachian rocks decreases to the NW and varies from about 0-5 km in our study area.

Receiver function studies within the Cumberland Plateau region of Tennessee show that crustal thickness is ~40-55 km (Owens *et al.*, 1984; Owens *et al.*, 1987). Other results have shown that there is no sharp Moho discontinuity, and that the Moho may be a laminated boundary (Owens *et al.*, 1984; Cook and Vasudevan, 2006).

Receiver function analyses from Wagner *et al.* (2010) show crustal thicknesses ranging from 47 km below the Blue Ridge province to 42 km below the Central Piedmont. Wagner *et al.* (2010) account for lateral heterogeneities within the basement by grouping receiver functions azimuthally. Baker (2006) shows receiver function results that indicate crustal thicknesses of ~48-52 km below the Blue Ridge province and ~39-42 km below the Carolina terrane. Azimuth variation shows that, at each location, crustal thickness decreases from NW to SE. $\frac{V_P}{V_S}$ is also calculated and is 1.742-1.852 in the Blue Ridge province and 1.720-1.777 in the Carolina terrane (Baker, 2006). These results are indicative of a granitic/intermediate composition within the Blue Ridge to a more granitic composition within the Carolina terrane (Christensen, 1996; Baker, 2006).

Wide-angled reflection techniques using regional quarry blasts yield crustal thicknesses of 47-51 km below the Blue Ridge to 38 km below the Carolina terrane (Hawman, 2008). Again, crustal thinning is in the southeast direction. Thicknesses from wide-angled reflection data agree well with those from receiver function studies.

Local earthquake tomography indicates that velocity changes abruptly across the vertical projection of the NY-AL magnetic lineament; low velocity is present to the northwest of the lineament while high velocity is present to the southeast (Figure 6). The low-velocity zone extends to at least 20 km depth. Relocated earthquake hypocenters occur within a depth range of 4-22 km. This correlates well with depth constraints presented by Chapman *et al.* (1997).

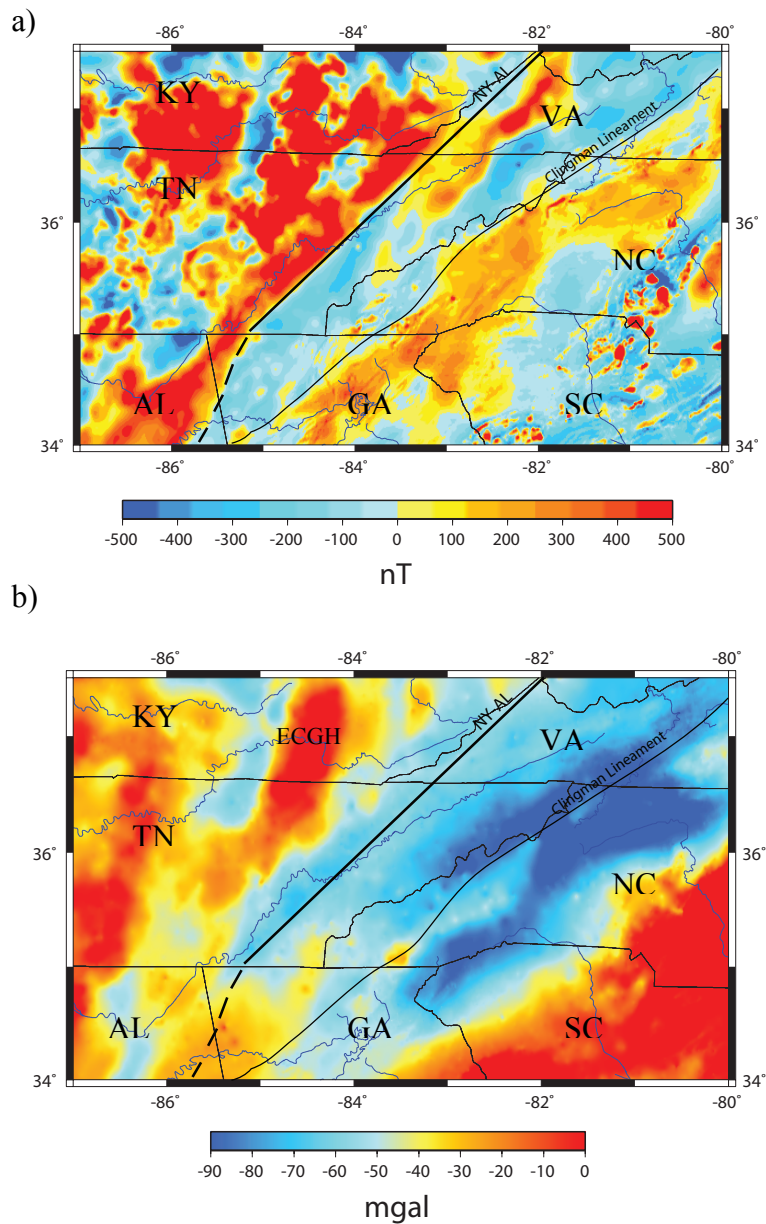


Figure 3: Magnetic and gravity anomalies within the ETSZ. The NY-AL lineament is labeled in each map. a) Magnetic anomaly map. Notice the high magnetic signature west of the lineament and the low magnetic signature east of the lineament. b) Bouguer gravity anomaly map. The gravity highs and lows correlated with the magnetic highs and lows in some places. However, in some instances, the potential fields are anticorrelated. An example is the gravity low associated with the NY-AL lineament magnetic high. Data obtained from GeoNet Gravity and Magnetic Dataset Repository from the University of Texas at El Paso (<http://irpsrvgis00.utep.edu/repositorywebsite>).

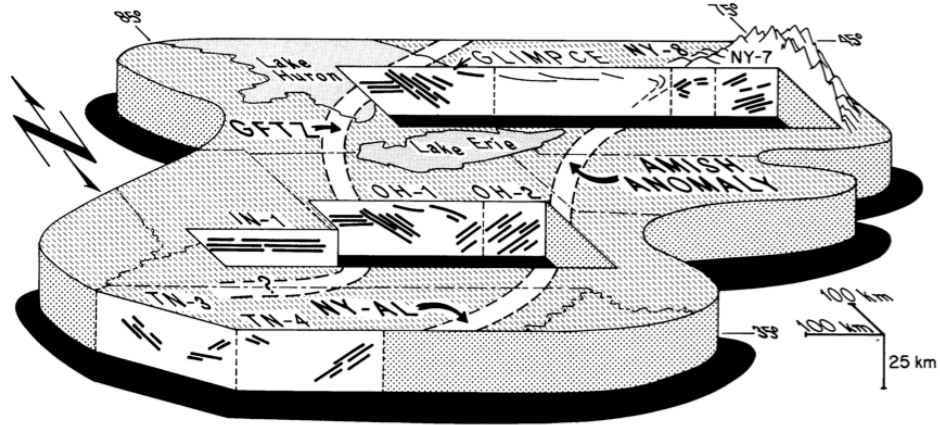


Figure 4: Map depicting locations of 8 seismic reflection lines from COCORP and the Great Lakes International Multidisciplinary Program on Crustal Evolution (GLIMPCE): TN-3, TN-4, IN-1, OH-1, OH-2, NY-7, and NY-8 from COCORP. GFTZ and the Amish Anomaly are appropriately labeled as the SW-NE trending lineaments. (from Culotta *et al.*, 1990).

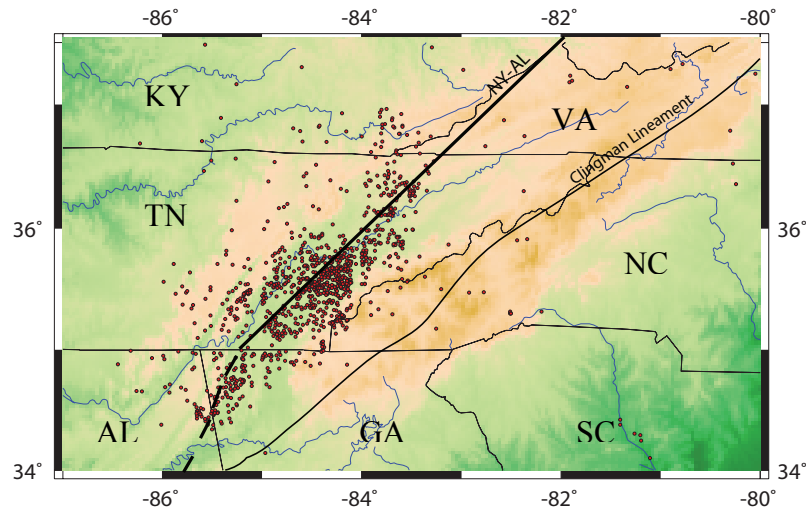


Figure 5: Map depicting local seismicity within the ETSZ. The NY-AL and Clingman lineaments are labeled above. Notice seismicity confined primarily to the SE side of the NY-AL lineament. 921 events from CERI *seisnet* database, spanning 1984-2009.

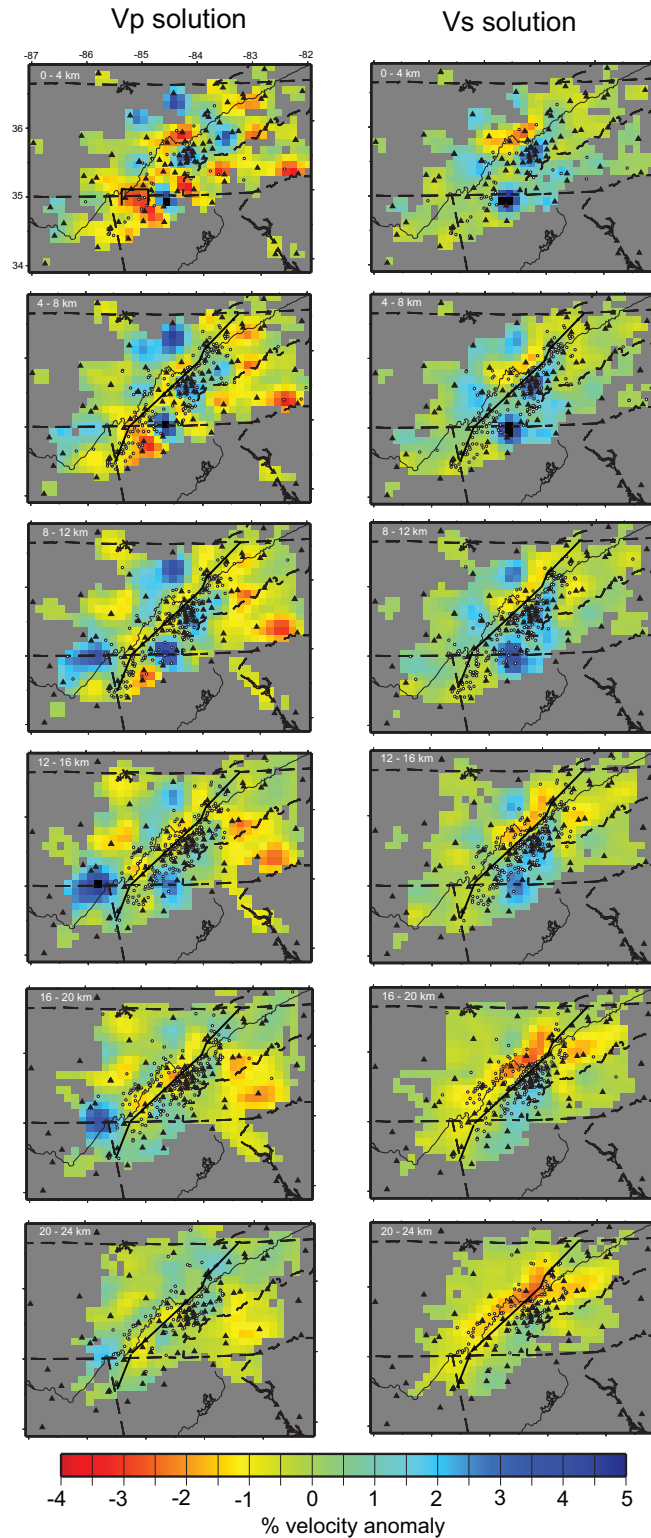


Figure 6: P-wave (left) and S-wave (right) velocity anomalies for the ETSZ. Slices in 4 km intervals. Red indicates low velocities and blue indicates high velocities. Notice at depth how P-wave velocities begin to lose resolution, but S-wave velocities intensify. (modified from Powell *et al.*, 2012).

An integrated study of COCORP acquisition lines from Tennessee to New York has identified the Grenville Front Transition Zone (GFTZ) and the NY-AL/Amish anomaly in several locations (Figure 4) (Culotta *et al.*, 1990). COCORP reflection lines within the GFTZ show eastward dipping structure while COCORP reflection lines crossing with the NY-AL/Amish anomaly show westward dipping structure. Correlation of the west-dipping structure with a boundary between two terranes containing magmatic-arc rocks in Canada suggests that the GFTZ/NY-AL/Amish anomaly zone represents a large intra-Grenville suture zone (Culotta *et al.*, 1990). In our study area, the location of the GFTZ is known only in the vicinity of the TN-KY border and is based upon the presence or absence of Grenville-aged metamorphism in drilled rock cores (Keller *et al.*, 1982). The front may exist close to the western edge of our study region (Figure 4; Figure 7).

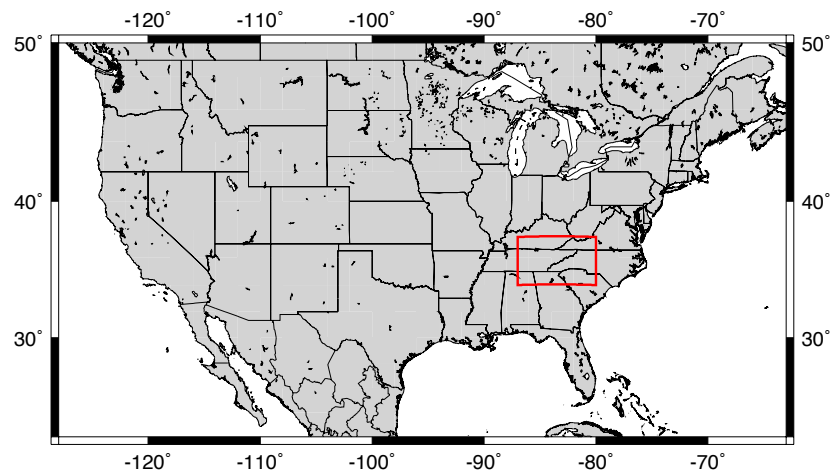


Figure 7: Map showing the outline of our study area. Study area is within the red box.

DATA AND DATA PROCESSING

Data for this study come from the University of Memphis' Center for Earthquake Research and Information (CERI). CERI operates and maintains a seismic network within the ETSZ (Figure 8). The network consists of 23 short-period and three broadband seismometers. We incorporate one additional station (TZTN) which is operated and maintained by the Incorporated Research Institutions for Seismology (IRIS) and is located in Tazewell, TN.

Events used must meet selection criteria in order to be used for this project. All events must be teleseismic with moment magnitudes greater than 6. They must be within an epicentral distance of 30° - 90° with focal depths greater than 30 km. Epicentral distances between 30° and 90° ensure simple mantle wave propagation and a near vertical arrival that has the potential for producing a strong Ps conversion at Moho depth. A total of 53 events are used for this study. Appendix A provides information for the events used. Figure 9 shows the location of these events and the distribution with respect to epicentral distance and azimuth.

A variety of instrument types exist throughout the eastern Tennessee seismic network. Short-period seismometers are either S-13 or L-4, and broadband seismometers are either Trillium-120 or STS2-I. The L-4 short-period seismometer stations are: CCNC, GFM, MGNC, RBNC, SMNC, TRYN, TVNC, and WSNC. The S-13 short-period seismometer stations are: ASTN, BCRT, BHT, CCRT, CMGA, CPRT, DYTN, ETT, GMG, GRBT, GTTN, LRVA, RCGA, VHTN, and WMTN. Station TZTN, maintained by IRIS, is an STS2-I, and the remaining broadband seismometers are Trillium-120.

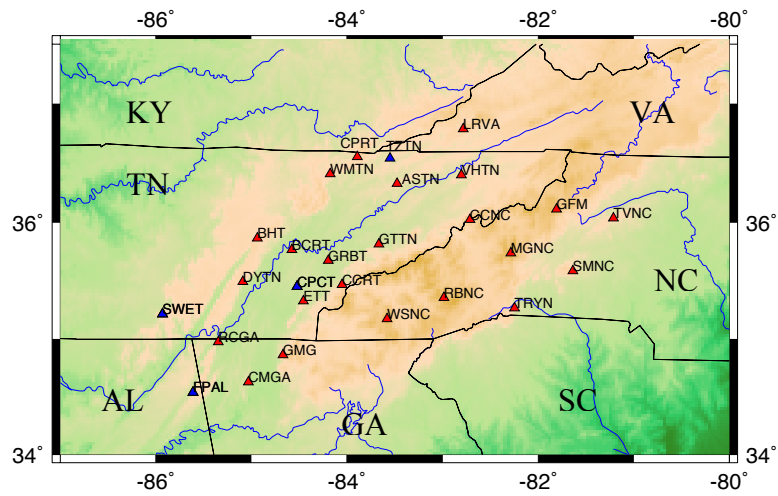


Figure 8: ETSZ network station map. Red stations have S-13 and L-4 short-period seismometers. Blue stations are broadband seismometers. The broadband station TZTN is maintained by IRIS. Stations' instruments are described previously.

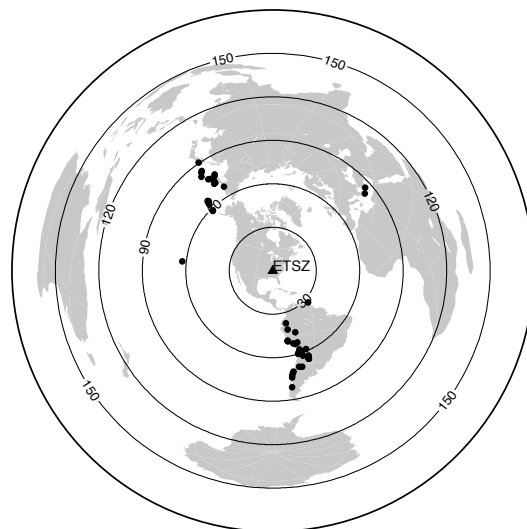


Figure 9: Map depicting events used in this study.

TRANSFER FUNCTIONS

Transfer function analysis can be used to image crustal and deeper interfaces where velocity contrasts produce Ps and/or Sp conversions (Figure 10) (Langston, 1979). Ideally, broadband seismometers are excellent at imaging upper mantle/lower crustal structures. Short-period seismometers reveal the presence of shallower crustal structure due to their higher frequency bandwidth (Langston, 1981; Jones and Phinney, 1998).

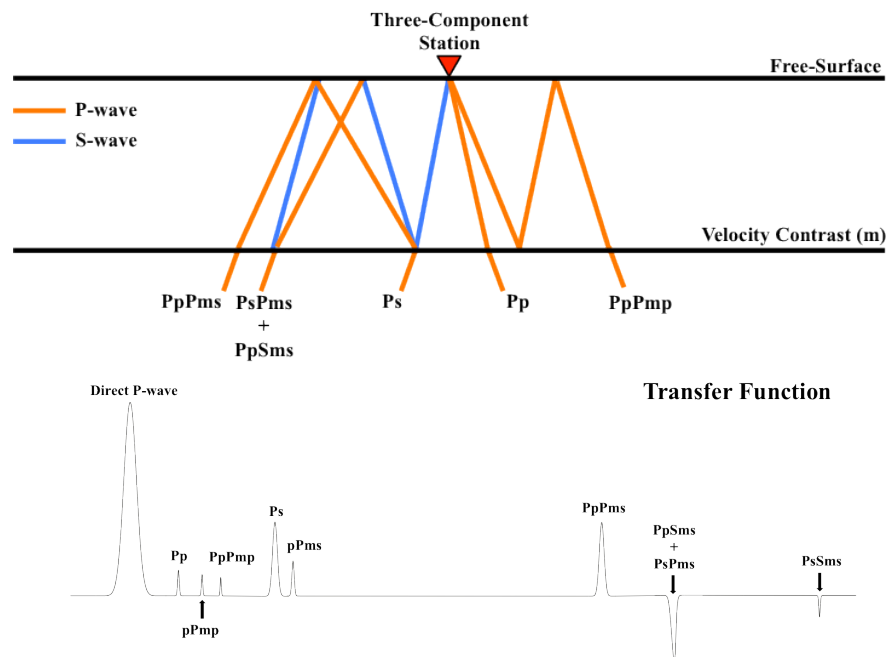


Figure 10: Transfer function ray diagram. Above shows the rays as they transmit through a boundary. Blue lines represent S waves. Orange lines represent P waves. Below shows the phases present in a transfer function. The phases in the transfer function can be seen in the diagram above it for any clarification. The Ps phase is the direct converted phase from a given boundary (namely the Moho), while the other phases are the multiples from that given boundary.

TRANSFER FUNCTION P-WAVE EQUALIZATION

The first step in transfer function analysis is to ensure that all stations share the same instrument response. This is done to satisfy criteria for a stacking method described below. All instrument responses were corrected to that of an S-13 short-period seismometer.

Transfer functions were created event-by-event using array stacking of vertical components (Langston and Hammer, 2001). Processing starts with the rotation of event N-S and E-W components into radial (away from source) and transverse (clockwise looking downward) motions. We assume that all vertical components will contain the same source wavelet for a given event since our area of interest is small relative to the distance to the earthquake. Stacking the vertical components will enhance that source wavelet and attenuate any random noise within the seismograms (Langston and Hammer, 2001). In order to stack the vertical components, a time shift is determined using cross correlation of a reference station to all other stations, and then the shifts are applied to every component to ensure that all seismograms are aligned properly. The reference station is determined separately for each event and is chosen visually. Once a vertical component stack is created (1), deconvolution can be performed to obtain the transfer functions.

$$S(t) = \frac{1}{N} \sum_{j=1}^N S_j(t + \tau_j) \quad j = 1, 2, 3, \dots, n \quad (1)$$

is the formulation for the vertical component stack, where $S(t)$ is the stack, N is the number of stations in the stack, $S_j(t)$ is the vertical component from the j^{th} station, and τ_j

is the relative time lag determined by cross correlation of a reference station vertical component with the vertical component from the j^{th} station.

We use a spectral “waterlevel” deconvolution from Langston (1979). A convolution model is assumed for each seismogram:

$$\begin{aligned} D_V(t) &= S(t) * E_V(t) \\ D_R(t) &= S(t) * E_R(t) \\ D_T(t) &= S(t) * E_T(t) \end{aligned} \quad (2)$$

where $D_V(t)$, $D_R(t)$, and $D_T(t)$ are the vertical, radial, and tangential seismograms. $S(t)$ is the stacked effective source function which also includes the S-13 instrument response, and $E(t)$ is the earth response.

Deconvolution is division in the frequency domain. Therefore, we can obtain vertical, radial, and tangential transfer functions in the frequency domain from

$$\begin{aligned} \widehat{E}_V(\omega) &= \frac{\widehat{D}_V(\omega)}{\widehat{S}(\omega)} \\ \widehat{E}_R(\omega) &= \frac{\widehat{D}_R(\omega)}{\widehat{S}(\omega)} \\ \widehat{E}_T(\omega) &= \frac{\widehat{D}_T(\omega)}{\widehat{S}(\omega)} \end{aligned} \quad (3)$$

Transforming these results back into the time domain will yield the transfer functions. However, these transfer functions will contain random noise. Before transforming into the time domain, high frequency noise can be attenuated by applying the transform of a Gaussian function, $G(\omega)$, to the deconvolution (Langston, 1979):

$$\widehat{E}_R(\omega) = \frac{\widehat{D}_R(\omega)\widehat{S}^*(\omega)}{\widehat{\phi}_{SS}(\omega)} \cdot G(\omega) \quad (4)$$

$$\widehat{\phi}_{SS}(\omega) = \max\{\widehat{S}(\omega)\widehat{S}^*(\omega), c \max[\widehat{S}(\omega)\widehat{S}^*(\omega)]\} \quad (5)$$

$$G(\omega) = e^{\frac{-\omega^2}{4\alpha^2}} \quad (6)$$

The asterisks denote complex conjugates. $\widehat{\phi}_{SS}(\omega)$ is the “waterlevel” deconvolution. The troughs of the spectrum are filled to a certain level depending on the constant c in order to avoid dividing by zero. For every deconvolution we assume $c = 0.04$ and $\alpha = 8$. α controls the width of the Gaussian function. Increasing the width of the Gaussian produces a lower-frequency estimate of the transfer functions (Ammon *et al.*, 1990).

The azimuthal variation of the earthquake data is small; most of our events occurred either along the Aleutian Islands-Kamchatka-Kuril Islands or in South America near Chile (Figure 9). Each station’s radial, tangential, and vertical component transfer function is a stack of all of the transfer functions that we computed for that given station. Table 1 shows how many waveforms are stacked for each station. The lack of waveforms in each stack is a result from either missing horizontal components, stations that were down, stations that had not been installed until the end of the time period of our dataset, and/or noisy data that resulted in bad transfer functions.

Radial component transfer functions were compared to their corresponding tangential component transfer functions in order to examine any strong wave scattering effects within the data. Scattered waves on the horizontal component, combined with amplitudes that equal those of the radial component, indicate strong large-scale crustal heterogeneities near a given station (Langston, 1989). Figures 11 and 12 show the radial and tangential component comparisons for each station within the ETSZ. A total of 13 stations were used in subsequent analysis (Figure 11). The remaining 11 stations were

not used due to apparently intense wave scattering (Figure 12). Stations FPAL, LRVA, and WSNC had no transfer functions.

Table 1: Table showing the number of waveforms within each stations' vertical, radial, and tangential transfer function stack.

Station	Vertical Waveforms	Radial Waveforms	Tangential Waveforms
ASTN	41	2	2
BCRT	51	51	51
BHT	41	41	41
CCNC	17	2	2
CCRT	34	34	34
CMGA	33	33	33
CPCT	43	43	43
CPRT	41	2	2
DYTN	49	49	49
ETT	48	48	48
FPAL	0	0	0
GFM	23	2	2
GMG	30	30	30
GRBT	38	38	38
GTN	45	2	2
LRVA	0	0	0
MGNC	32	2	2
RBNC	27	1	1
RCGA	51	51	51
SMNC	17	1	1
SWET	37	36	36
TRYN	19	1	1
TVNC	5	1	1
TZTN	35	35	35
VHTN	21	1	1
WMTN	42	2	2
WSNC	0	0	0

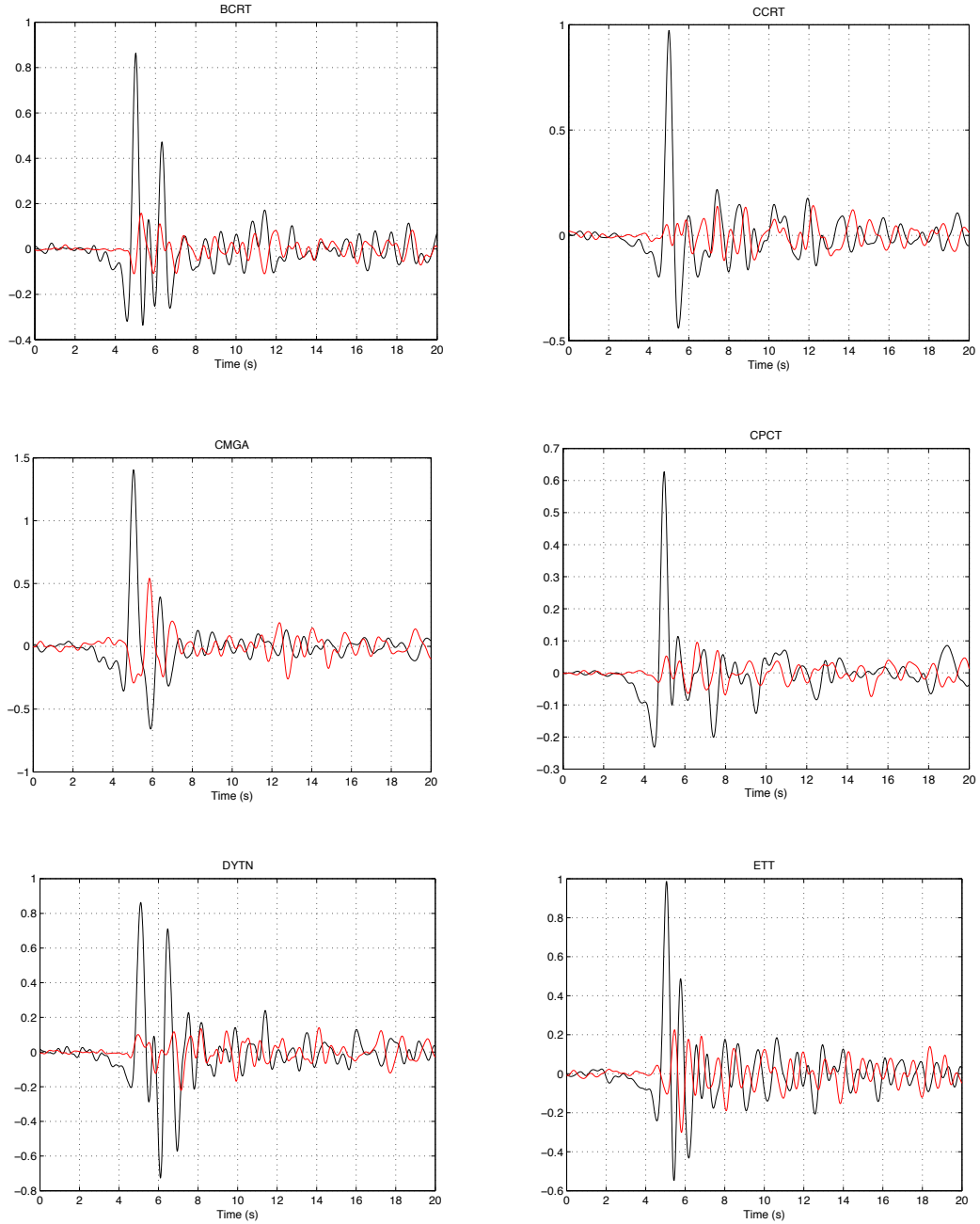


Figure 11: Radial and tangential component transfer function comparison. Both radial and tangential waveforms are stacks. Black line represents the radial component. Red line represents the tangential component. These stations yield acceptable inversion results.

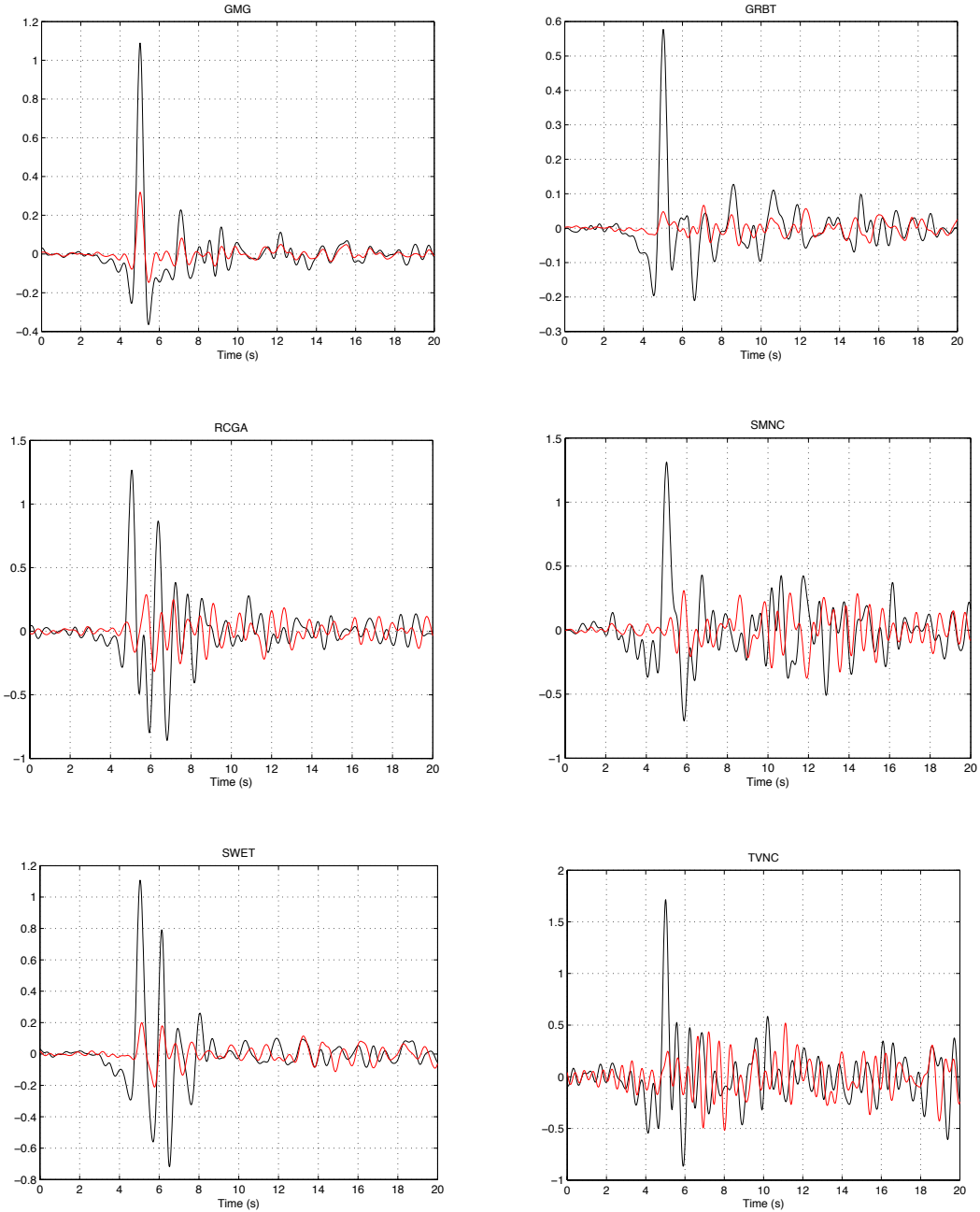


Figure 11 cont.: Radial and tangential component transfer function comparison. Both radial and tangential waveforms are stacks. Black line represents the radial component. Red line represents the tangential component. These stations yield acceptable inversion results.

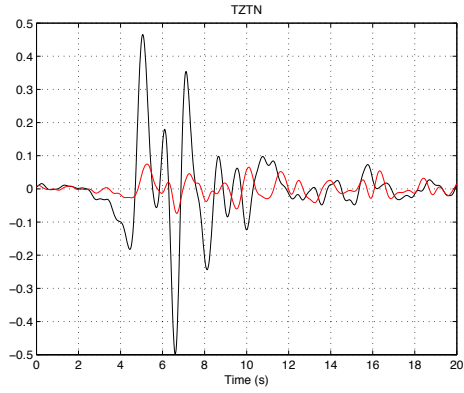


Figure 11 cont.: Radial and tangential component transfer function comparison. Both radial and tangential waveforms are stacks. Black line represents the radial component. Red line represents the tangential component. These stations yield acceptable inversion results.

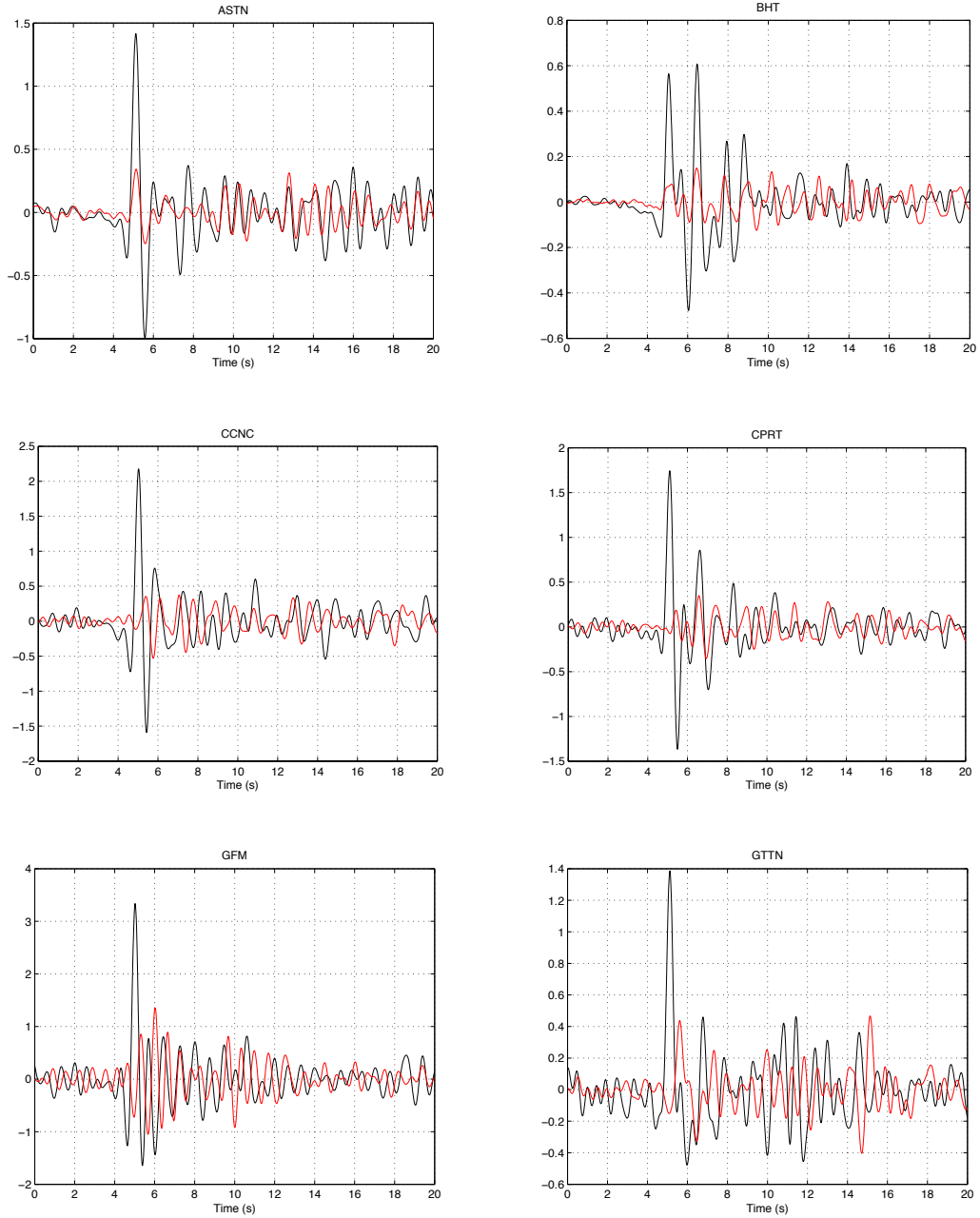


Figure 12: Radial and tangential component transfer function comparison. Both radial and tangential waveforms are stacks. Black line represents the radial component. Red line represents the tangential component. These stations yield inconsistent inversion results and bad waveform fits.

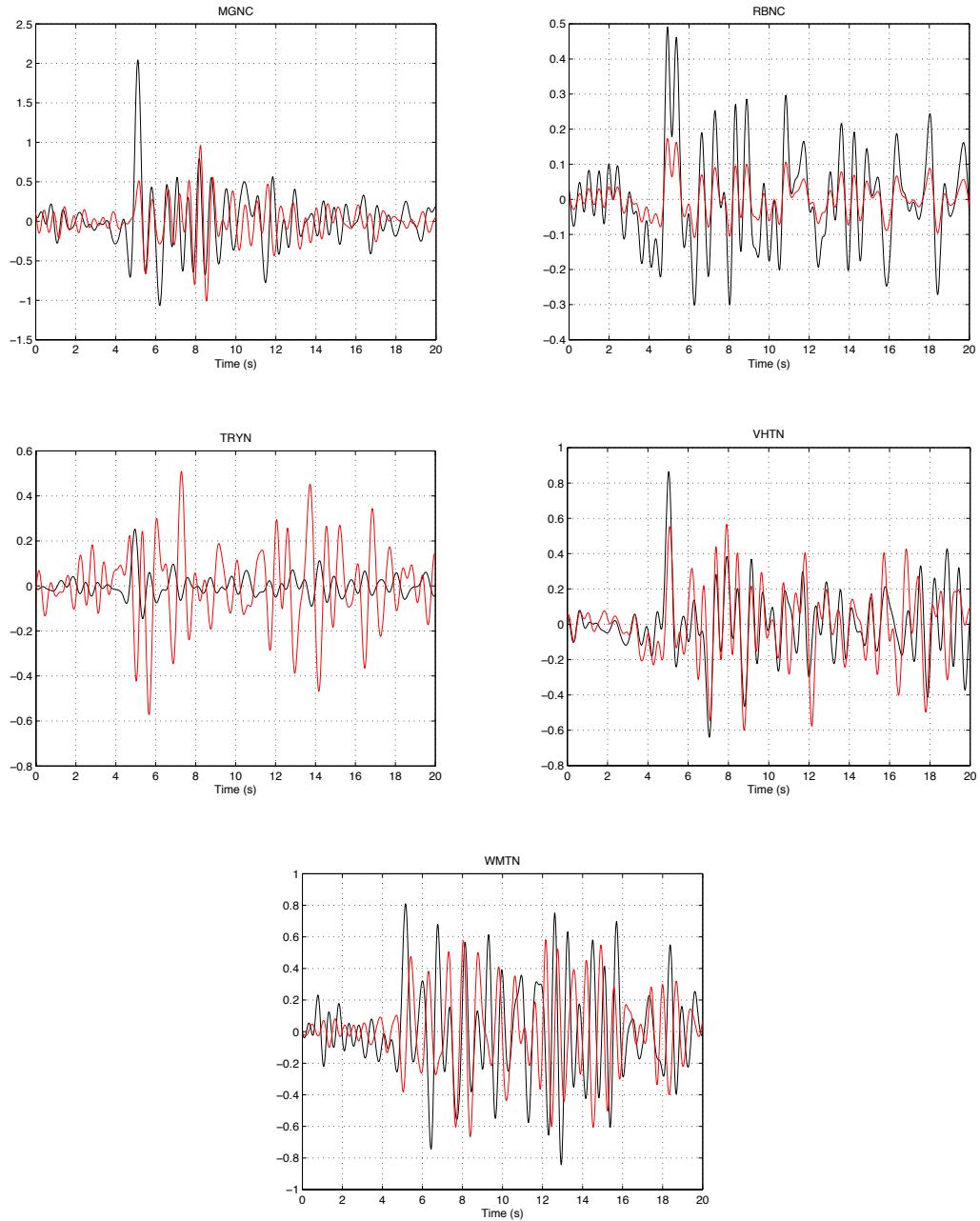


Figure 12 cont.: Radial and tangential component transfer function comparison. Both radial and tangential waveforms are stacks. Black line represents the radial component. Red line represents the tangential component. These stations yield inconsistent inversion results and bad waveform fits.

WAVEFORM INVERSION

An inversion of the radial component transfer function is performed to obtain a one dimensional velocity model beneath each station. ET1D, a one dimensional model (Figure 13; Table 2), is used as the initial starting model (Vlahovic *et al.*, 1998). A more reasonable starting model was obtained, through forward modeling, by altering the values of ET1D and creating synthetics and then comparing the synthetics to the data (radial component transfer function) at station CMGA (Figure 14; Table 3). CMGA was chosen because it has a relatively simple waveform, but still contains the complexity of typical short-period signals. Being able to match a starting model to CMGA's radial component transfer function gives us some confidence that our velocity inversions will be meaningful. V_P and/or V_S are approximated using $\frac{V_P}{V_S} \approx \sqrt{3}$. Density is approximated by $\rho \approx 1.74(V_P^{0.25})$ (Brocher, 2005).

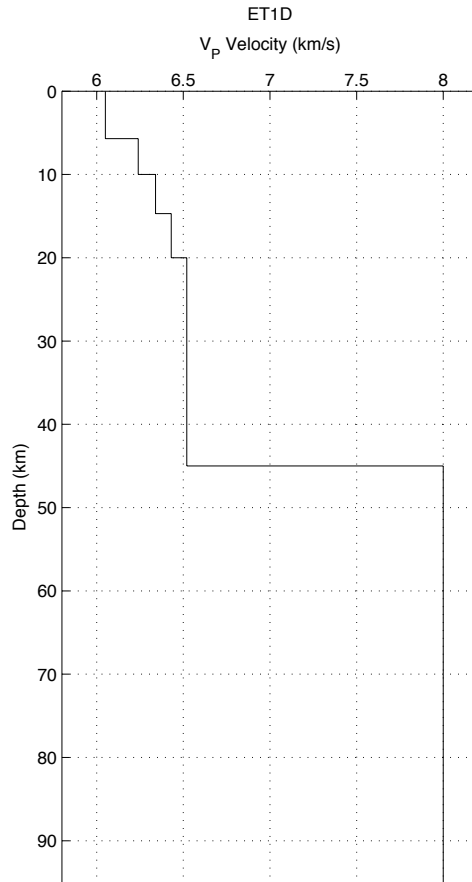


Figure 13: Initial velocity model, ET1D. Values in Table 2. (from Vlahovic *et al.*, 1998).

Table 2: Values for initial model ET1D. Velocities are in km/s, density in g/cc, and thickness is in km. (from Vlahovic *et al.*, 1998).

V_P	V_S	ρ	<i>thickness</i>	Q_P	Q_S
6.05	3.47	2.223	5.7	500.0	250.0
6.24	3.59	2.240	4.3	500.0	250.0
6.34	3.66	2.249	4.7	500.0	250.0
6.43	3.72	2.257	5.3	500.0	250.0
6.52	3.79	2.267	25.0	500.0	250.0
8.00	4.62	2.368	50.0	500.0	250.0

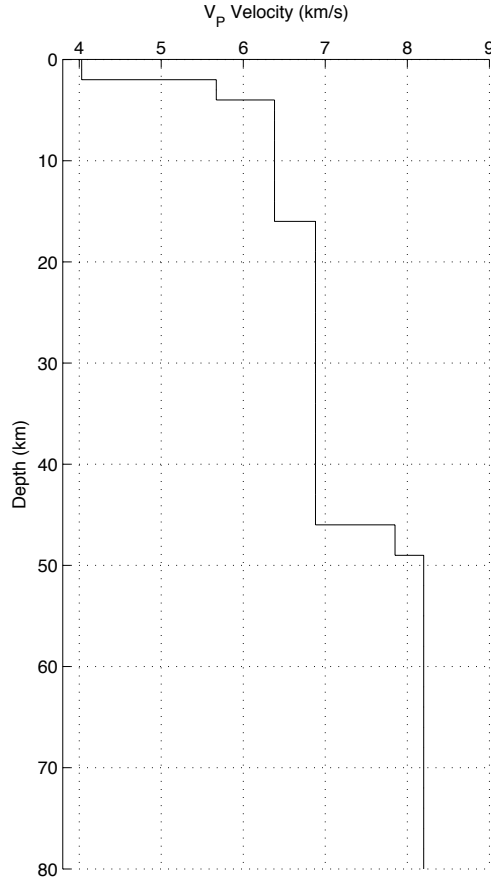


Figure 14: Initial model used in inversions. Values in Table 3. Model was created by the forward modeling technique described earlier.

Table 3: Values for modified ET1D that is used in our inversions. Velocities are in km/s, density in g/cc, and thickness is in km.

V_P	V_S	ρ	<i>thickness</i>	Q_P	Q_S
4.03	2.33	2.059	2.0	500.0	250.0
5.67	3.27	2.584	2.0	500.0	250.0
6.38	3.68	2.811	12.0	500.0	250.0
6.88	3.97	2.971	30.0	500.0	250.0
7.85	4.53	3.282	3.0	500.0	250.0
8.20	4.73	3.394	31.0	500.0	250.0

An Occam's inversion is used to create new velocity models for each station within the ETSZ (Ammon *et al.*, 1990; Constable *et al.*, 1987). From Ammon *et al.* (1990), the forward problem is described by

$$d_j = F_j[\mathbf{m}] \quad j = 1, 2, 3, \dots, N, \quad (7)$$

where d_j is the data out to N data points, and F_j is the operator which works on the model \mathbf{m} . This relationship is inherently non-linear. However, it can be linearized by expanding it in a Taylor series about an initial model:

$$F_j[\mathbf{m}] = F_j[\mathbf{m}_0] + (\mathbf{D}, \delta\mathbf{m})_j + O\|\delta\mathbf{m}^2\|, \quad (8)$$

where $(\mathbf{D}, \delta\mathbf{m})$ is the inner product of matrix \mathbf{D} . Matrix \mathbf{D} is the m by n partial derivative matrix of the operator F on \mathbf{m}_0 . m is the number of data points, and n is the number of layers in the model. The term $O\|\delta\mathbf{m}^2\|$ describes the remainder term in the Taylor's expansion and that it is of second order in the model perturbation. Equation (8) is still non-linear, but removing the last term linearizes the system and gives

$$(\mathbf{D}, \delta\mathbf{m})_j \approx F_j[\mathbf{m}] - F_j[\mathbf{m}_0]. \quad (9)$$

The right hand side of this equation is the residual vector. Performing an inversion by minimizing the L_2 norm here would result in acceptable model changes. However, Constable *et al.* (1987) describe a method that solves for model parameters instead of model parameter perturbations. By adding $(\mathbf{D}, \mathbf{m}_0)$ to both sides of the last equation, we can solve directly for a new \mathbf{m} vector.

$$(\mathbf{D}, \mathbf{m})_j \approx d_j - F_j[\mathbf{m}_0] + (\mathbf{D}, \mathbf{m}_0)_j. \quad (10)$$

This inversion can be stabilized and constrained by *a priori* velocity constraints through the addition of smoothing equations to the system. This is similar to damping, in that we minimize the model roughness norm by minimizing the first derivative of the model. We accomplish this by adding $\sigma\boldsymbol{\Psi} = \mathbf{0}$ to the system by

$$\begin{bmatrix} \mathbf{D} \\ \sigma\boldsymbol{\Psi} \end{bmatrix} \mathbf{m} \approx \begin{bmatrix} d_j \\ \mathbf{0} \end{bmatrix} - \begin{bmatrix} F_j[\mathbf{m}_0] \\ \mathbf{0} \end{bmatrix} + \begin{bmatrix} \mathbf{D}\mathbf{m}_0 \\ \mathbf{0} \end{bmatrix}. \quad (11)$$

The matrix $\boldsymbol{\Psi}$ represents the first difference of adjacent layers in the model.

$$\boldsymbol{\Psi} = \begin{bmatrix} 1 & -1 & 0 & 0 & \dots \\ 0 & 1 & -1 & 0 & \dots \\ 0 & 0 & 1 & -1 & \dots \\ 0 & 0 & 0 & 1 & \dots \\ \vdots & \vdots & \vdots & \vdots & \dots \end{bmatrix}, \quad (12)$$

where, since \mathbf{D} is an m by n matrix, $\boldsymbol{\Psi}$ is a p by n matrix so that $m \geq n \geq p$ and p is the number of layers within the model. The constant, σ , scales the effect that the first derivative will have on the inversion.

The partial derivatives in \mathbf{D} are computed using finite differences of the forward model and the forward model with each layer perturbed by 2.5% of its original value.

The general form of the partial derivative matrix is

$$D = \begin{bmatrix} \frac{\partial f_1(m)}{\partial m_1} & \dots & \frac{\partial f_1(m)}{\partial m_n} \\ \vdots & \ddots & \vdots \\ \frac{\partial f_m(m)}{\partial m_1} & \dots & \frac{\partial f_m(m)}{\partial m_n} \end{bmatrix} \quad (13)$$

where a first order finite difference approximation is assumed by

$$\frac{\partial D(\mathbf{m})_j}{\partial m_j} \approx \frac{R_{syn}(V_S) + R_{syn}(V_S + \delta V_S)}{-\delta V_S} \quad j = 1, 2, 3, \dots, N. \quad (14)$$

The matrix D is an m by n matrix, where m is the number of data points (N), and n is the number of layers within the model. R_{syn} is the synthetic seismogram created from the forward problem, and δV_S is the amount of change from the perturbation of a specific layer's value.

Waveform fitting can be difficult, and one must remember that the smoothest model does not always result in a quality fit, and a quality fit does not always come from the smoothest model. There is always a trade-off. For this project, we perform a suite of inversions with varying σ 's: from 0.6-1.8. The tolerance cut-off for the inversion is when the residual difference between iterations is less than 0.001. Most inversions converge within four or five iterations. We use a ray parameter of 0.06 for our synthetics, which is comparable to an event about 60° away in epicentral distance. We choose this ray parameter because our transfer functions are stacks of all of the events, and 0.06 is a good average of them. Ray parameter is used in our synthetic seismogram calculations and is used to find the incidence angle of the ray through a propagator matrix.

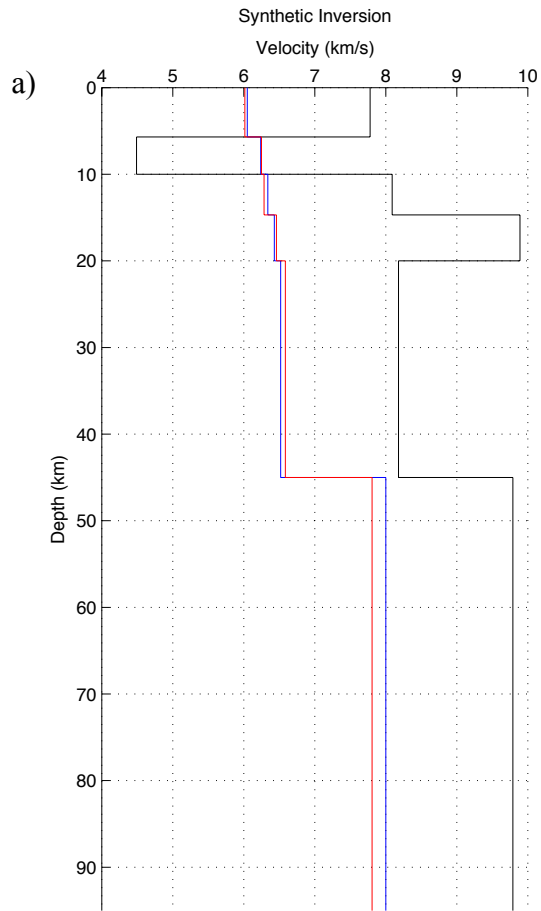
Absolute amplitude is a problem when inverting waveforms. Our synthetics are, for the most part, larger in amplitude than the data are. Amplitude control is crucial to the stability of the inversion. The amplitudes of the synthetic waveforms throughout the inversion iterations are scaled using

$$R_{syn} = \frac{R_{syn}[\max\{d\}]}{\max\{R_{syn}\}} \quad (15)$$

where d is the data waveform. This forces the synthetic seismogram's maximum amplitude to be scaled to the amplitude of the data.

SYNTHETIC INVERSION

To check the accuracy of our inversion we invert synthetics created with a known velocity model to see if we can get our initial parameters back out of the inversion. For this we created 10 synthetic seismograms using ET1D (Figure 13; Table 2). The seismograms were created using varying ray parameters equivalent to epicentral distances of 30°-90°. These waveforms were then stacked to emulate our stacks of data within the actual inversions. After creating our “data” (stack of synthetic seismograms), we perturbed ET1D drastically to change its effect on any newly created synthetic seismograms. This perturbed earth model is now our starting model for the inversion. Using the methods above, and a σ of 0.5, we were able to obtain the original waveform fit and earth model after 7 iterations. Figure 15 shows the waveform fits and the associated earth models for this synthetic inversion. We were able to fit the waveform nearly perfectly to the “data,” and our final model agrees very well with the original ET1D earth model. These results increase our confidence with our inversion technique and program.



b)

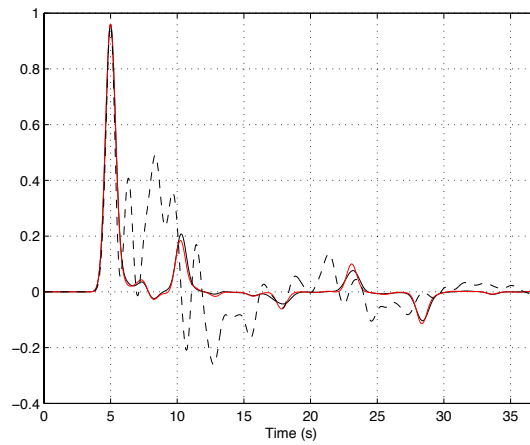


Figure 15: Results from a synthetic inversion. a) V_p profiles for the initial model (black), the final model (red), and ET1D (blue). b) Waveforms associated with the inversion. Black line is the synthetic stack created using ET1D. Red line is the final waveform from the inversion. Dashed line is the synthetic seismogram from the initial model.

RESULTS

Results yield acceptable waveform fits to the data with reasonable earth models. Figure 16 shows the waveform fits of each inversion performed at the 13 stations used in the study. The inversions generally fit very well within the first 13 seconds and begin to fail past that. Scattering is suggested because the amplitude of the radial component matches that of the tangential component beginning at around 13 seconds (Figure 11).

Earth models were obtained for each individual station. Figure 17 shows the P-wave velocity profiles for each of the inversions. We invert for V_S , however it is more customary to display velocities in V_P . V_P is overall easier to understand and is better known to most people. Each suite of inversions represents results from a range of smoothing parameters. An indication of the variance in each layer is provided by the spread of the inversion results. These are simply ranges for what the velocity of any given layer could be. While the true velocity value is a goal for this project, we are more interested in the trends of velocities within the earth models. Appendix B shows the averages, maximums, and minimums for each layer in each station's suite of inversions. These ranges for portions of the velocity models capture what could be true velocities in the subsurface. The areas where all of the inversions are very close together are areas where we are able to resolve earth structure very well and are probably a good indicator of true velocity. It is difficult to say which smoothing parameter at each station creates the "correct" model. This is why we have performed several inversions at each station to show the ranges possible.

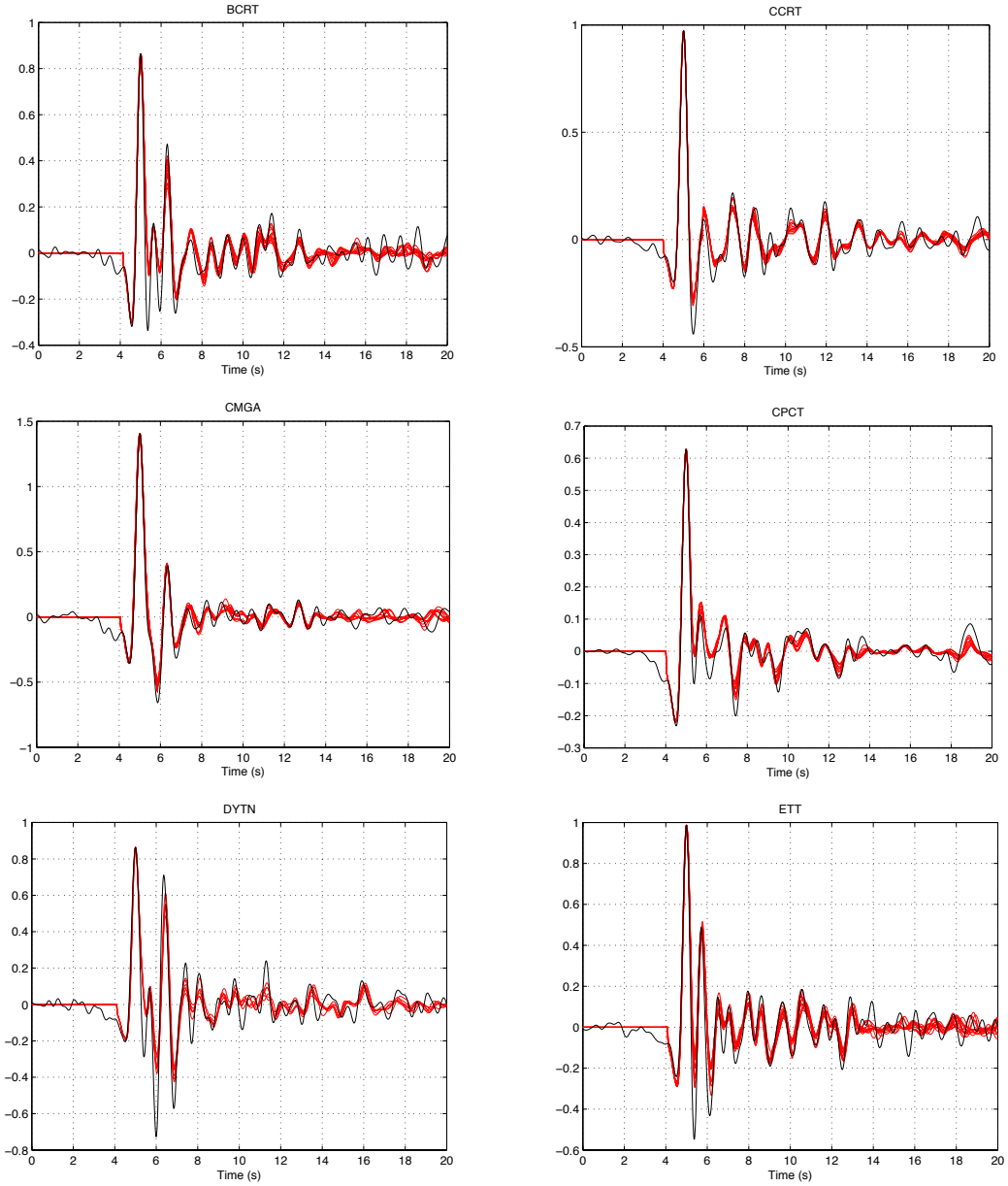


Figure 16: Waveform inversion results from stations BCRT, CCRT, CMGA, CPCT, DYTN, and ETT. Waveforms inverted are stacked waveforms. Black line represents the radial receiver function data. Red lines represent the inversion results with varying smoothing constraints.

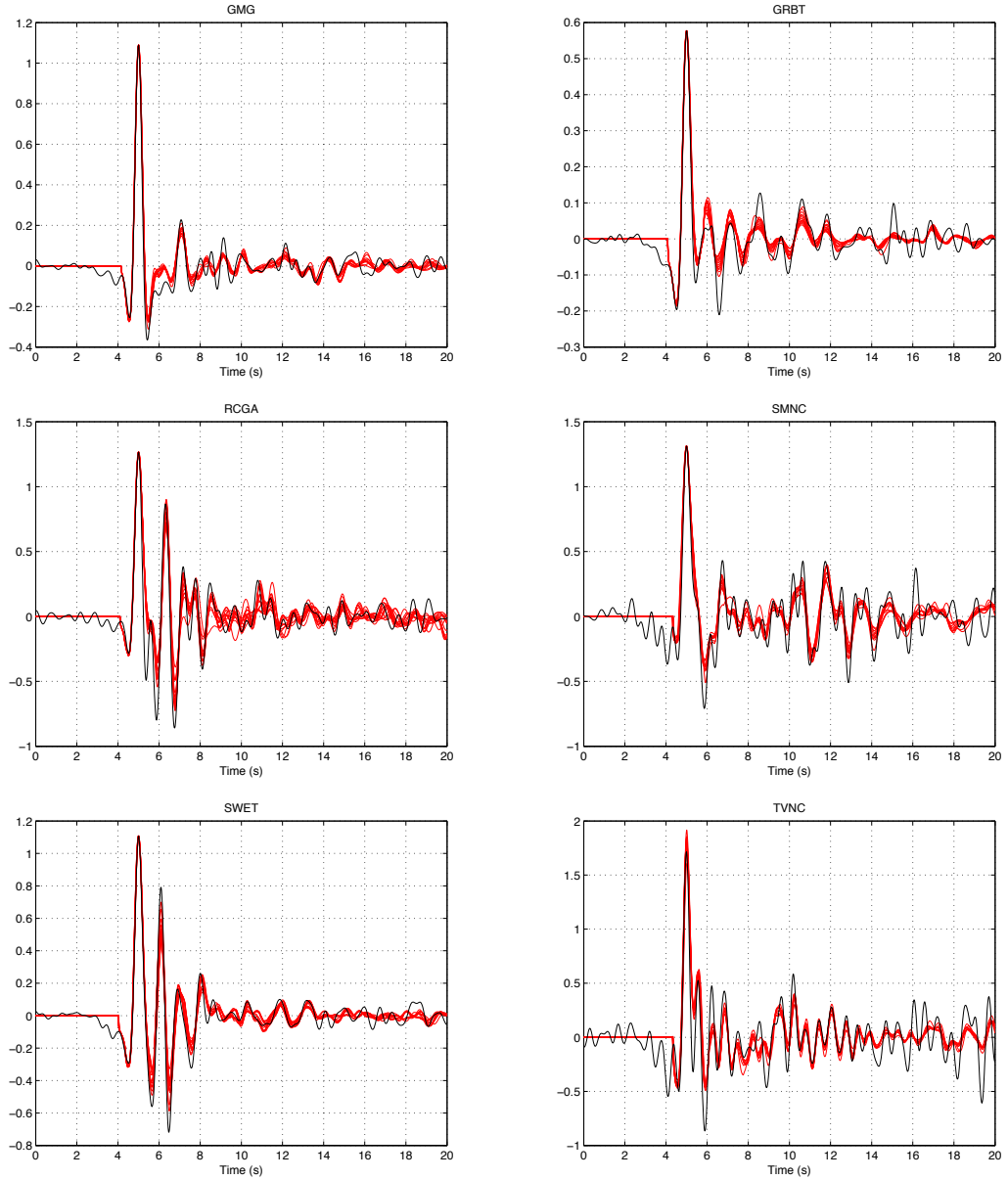


Figure 16 cont.: Waveform inversion results from stations GMG, GRBT, RCGA, SMNC, SWET, and TVNC. Waveforms inverted are stacked waveforms. Black line represents the radial receiver function data. Red lines represent the inversion results with varying smoothing constraints.

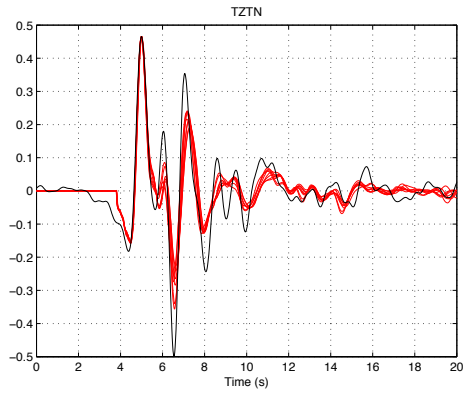


Figure 16 cont.: Waveform inversion result from station TZTN. Waveform is a stacked waveform. Black line represents the radial receiver function data. Red lines represent the inversion results with varying smoothing constraints.

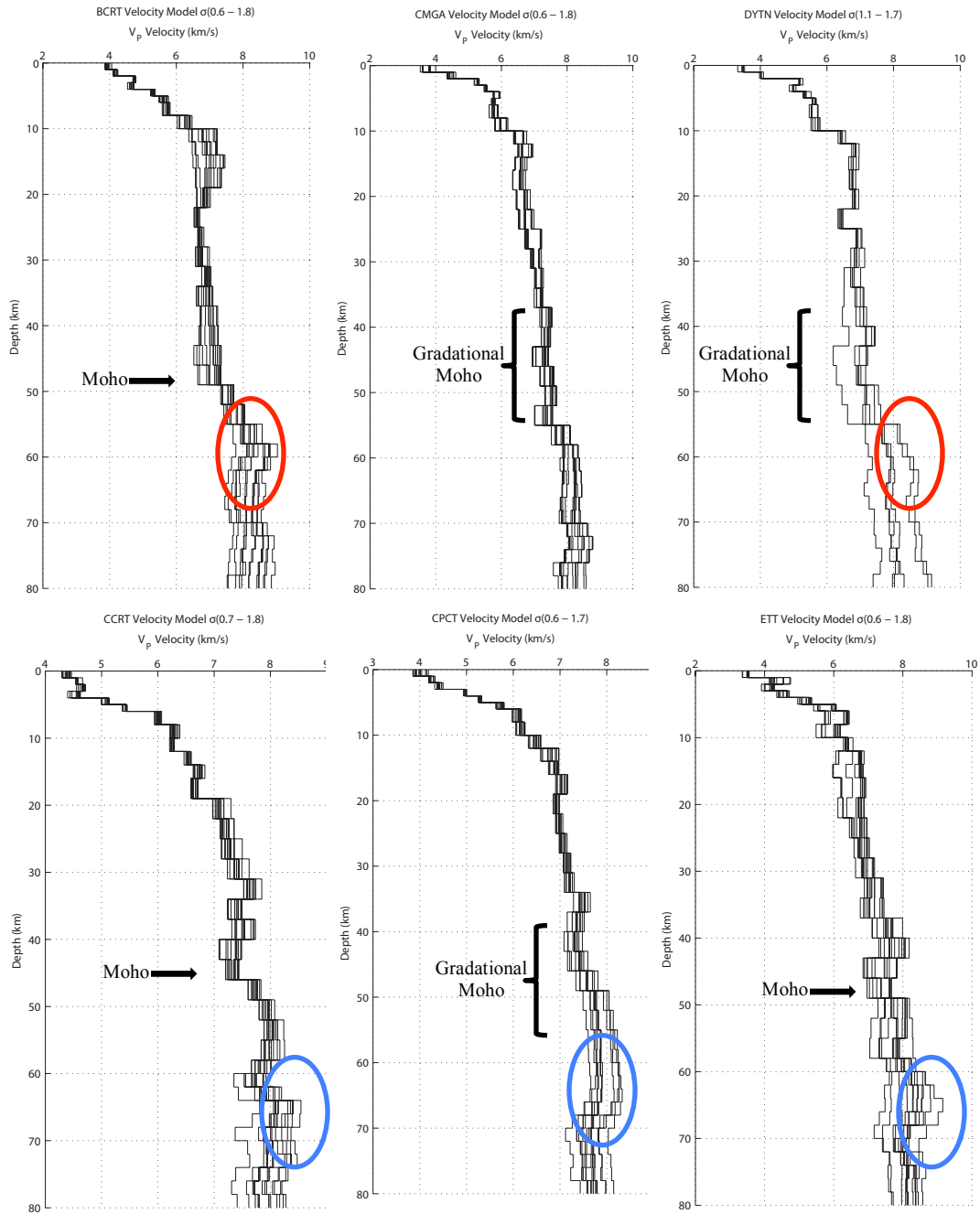


Figure 17: P-wave velocity profiles for stations BCRT, CCRT, CMGA, CPCT, DYT, and ETT. Each inversion is the result of using a different smoothing parameter. Range of smoothing parameters is labeled above each profile and increases 0.1 for each inversion. Moho and any gradational Moho is labeled. Red circles represent the 60 km depth high velocity zone. Blue circles represent the 65 km depth high velocity zone.

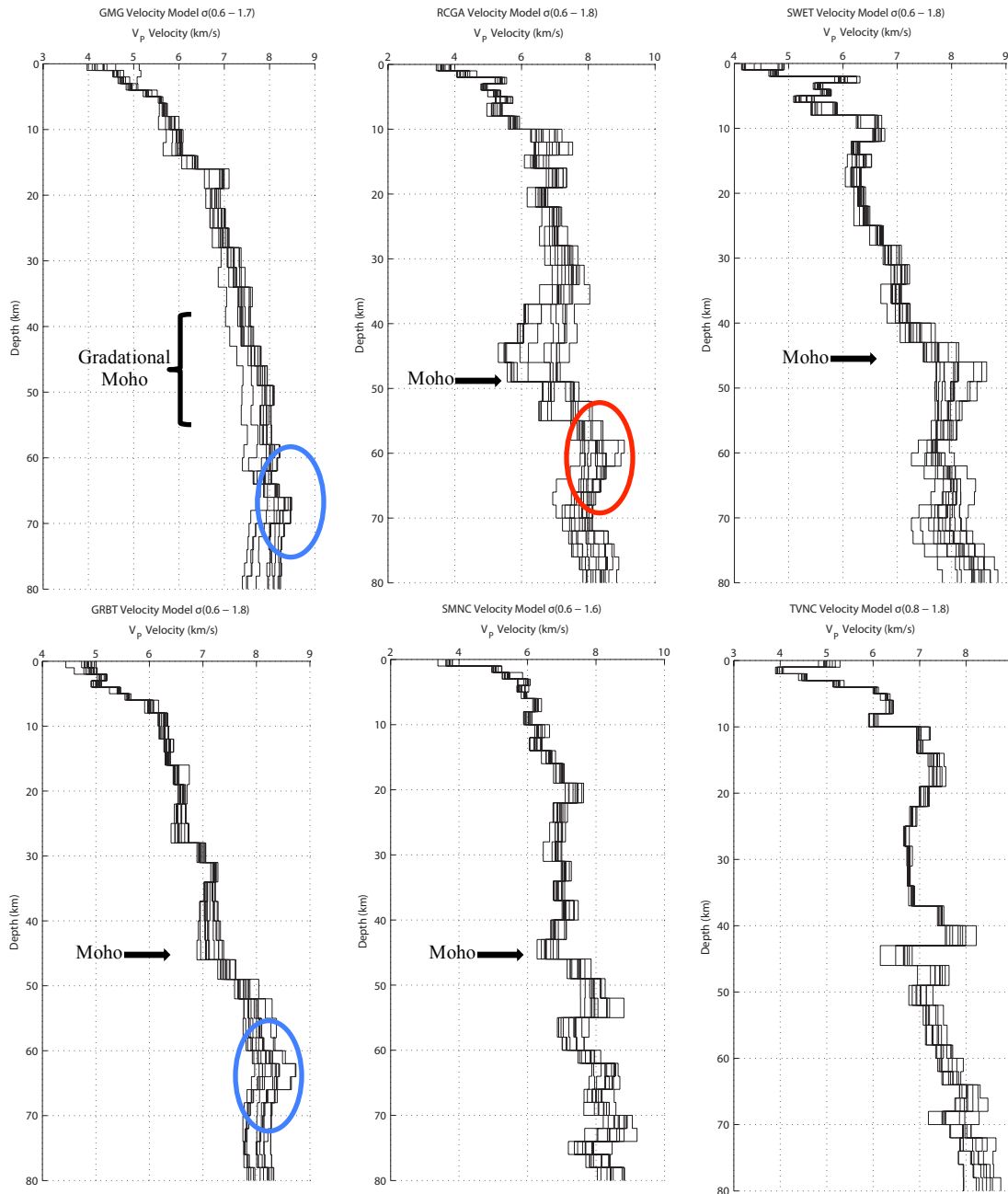


Figure 17 cont.: P-wave velocity profiles for stations GMG, GRBT, RCGA, SMNC, SWET, and TVNC. Each inversion is the result of using a different smoothing parameter. Range of smoothing parameters is labeled above each profile and increases 0.1 for each inversion. Moho and any gradational Moho is labeled. Red circles represent the 60 km depth high velocity zone. Blue circles represent the 65 km depth high velocity zone.

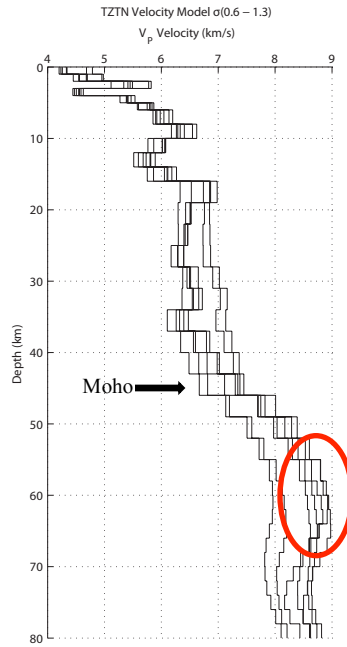


Figure 17 cont.: P-wave velocity profile for station TZTN. Each inversion is the result of using a different smoothing parameter. Range of smoothing parameters is labeled above the profile and increases 0.1 for each inversion. Moho and any gradational Moho is labeled. Red circles represent the 60 km depth high velocity zone. Blue circles represent the 65 km depth high velocity zone.

COMPARISON AGAINST A BROADBAND SEISMOMETER

An inversion was done for a single event recorded by broadband seismometers and short-period seismometers in order to see similarities and/or differences in the velocity model. An event on February 16, 2008 in Potosi, Bolivia was used for this calculation. One short-period and one broadband radial component transfer function were computed for stations CPCT, SWET, and TZTN. The alpha value for the short-period calculations was 8, and the alpha value for the broadband calculations was 3. Figure 18 shows the similarities and differences between the two methods at each station.

Overall, the general trend of both the broadband and short-period inversions is very similar. The greatest differences occur for station TZTN; the upper 10 km of the velocity profiles approximately agree, but the deeper features are different. The short-period inversion has higher velocities at depth overall, but one can still see a high velocity layer at 65 km depth on both inversions. At CPCT and SWET we see the same high and low velocity zones in each velocity profile. The short-period inversion results show a little more detail within those high and low velocity zones. Figures 18g and 18h illustrate this well. The high velocity zone at ~65 km depth is seen in both profiles. However, in Figure 18h we see a slight decrease in velocity just below the high velocity zone that is not seen in Figure 18g.

Inverting both broadband and short-period data also allows us to constrain our results. For the most part, the upper 10 km of both the broadband and the short-period inversion results agree.

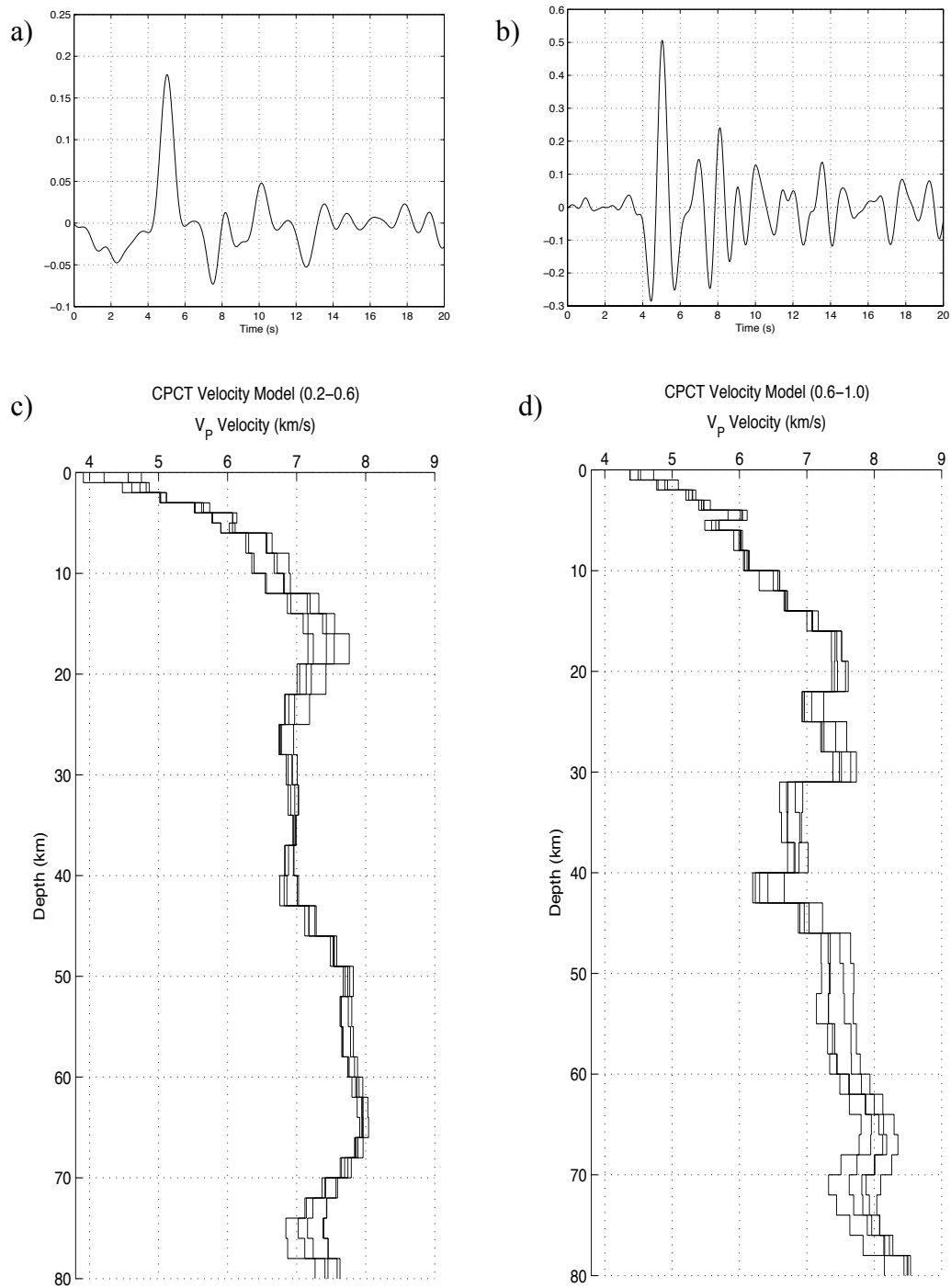


Figure 18: Comparison between the broadband and short-period methodologies at station CPCT. Event from 02/16/2008 in Potosi, Bolivia. a) Broadband radial component transfer function. b) Short-period radial component transfer function. c) Broadband inversion results (P-wave profile). d) Short-period inversion results (P-wave profile).

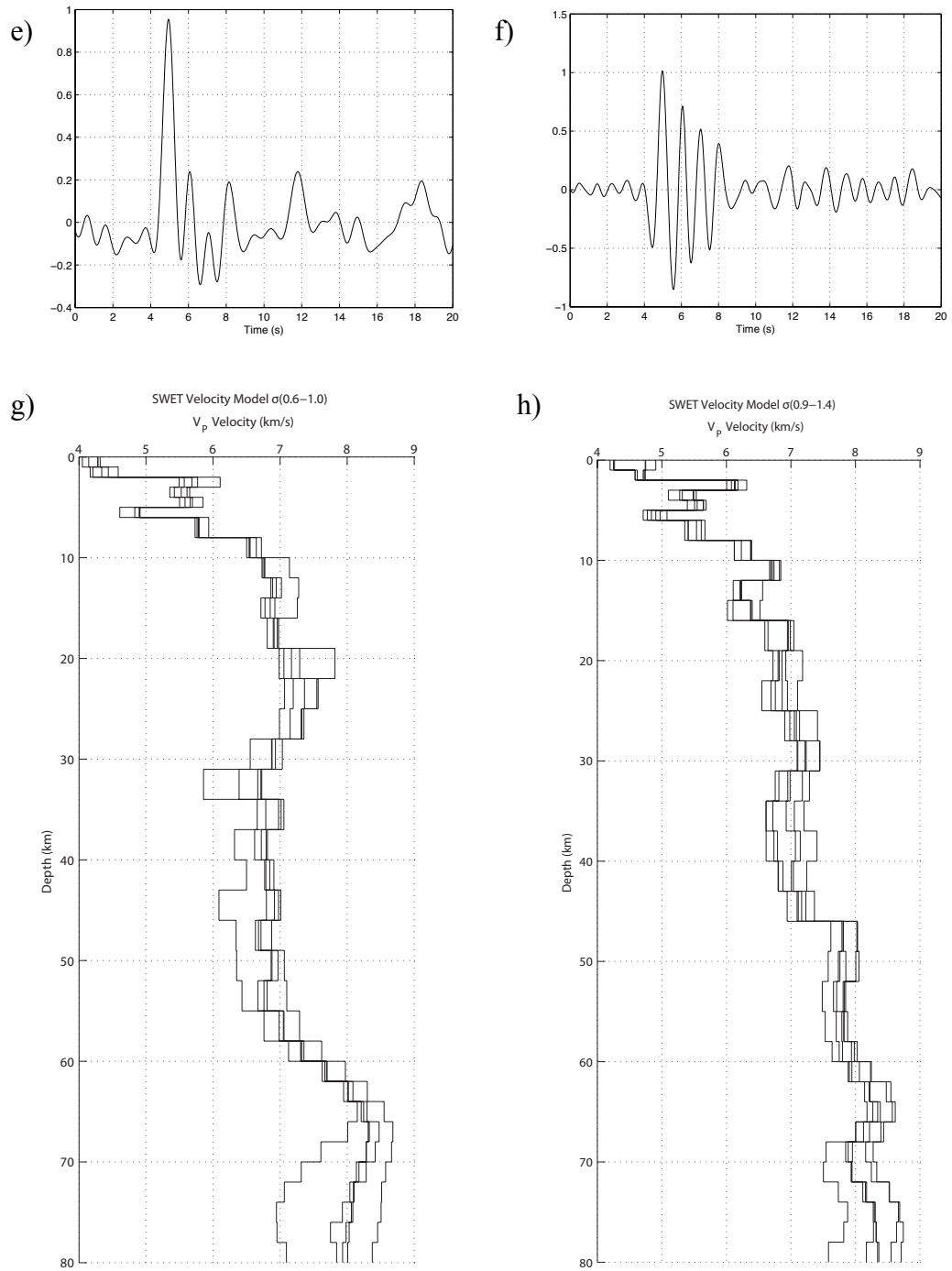


Figure 18 cont.: Results from station SWET. e) Broadband radial component transfer function. f) Short-period radial component transfer function. g) Broadband inversion results (P-wave profile). h) Short-period inversion results (P-wave profile).

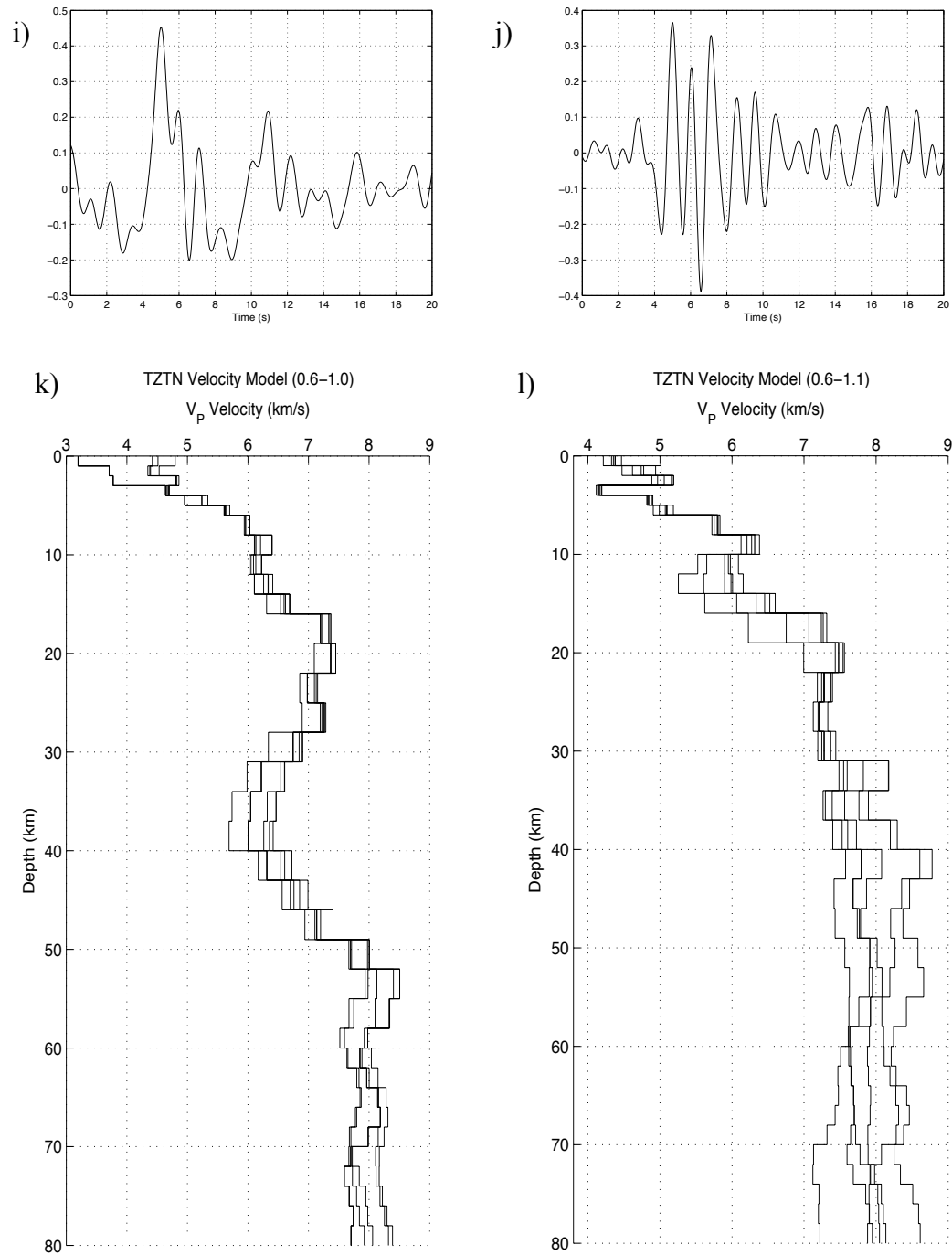


Figure 18 cont.: Results from station TZTN. i) Broadband radial component transfer function. j) Short-period radial component transfer function. k) Broadband inversion results (P-wave profile). l) Short-period inversion results (P-wave profile).

DISCUSSION

Our results provide new insight into the subsurface features of the ETSZ. Moho depths in the region are difficult to decipher. In many places the Moho is quite gradational, and in others it is visible as an abrupt increase in velocity. Figures 17 and 19a illustrate the locations of Moho depth at some stations within the ETSZ. Stations BCRT, CCRT, ETT, GRBT, SMNC, SWET, TVNC, and TZTN show an arguable Moho break in velocity in Figure 17. Other stations mostly show a gradational or laminated boundary making any Moho break difficult to determine. Laminated Moho boundaries are thought to be thin layered structures and have not been adequately studied. Hypotheses for a laminated Moho boundary are: relatively undeformed metasediments, cumulate layering, tectonic banding, and lenses of partial melt (Hale and Thompson, 1982). Meissner (1973) proposes layers of partial melt, crystallization seams, intrusions, and the peeling of mantle matter for a stepwise increase in velocity across a Moho boundary. Systematic variations in Moho depth are not observed, and variation in Moho depth is very limited. While stations like BCRT, CMGA, and TZTN show a very laminated boundary at Moho depths, stations CCRT and SMNC show a distinct Moho boundary around 46 km. This is comparable to results from other receiver function studies indicating that the Moho in central Tennessee is within a laminated zone of 40-55 km depth (Owens *et al.*, 1984).

Past studies have involved broadband radial component receiver functions, and we have shown that the broadband receiver function and the short-period transfer function for a given station are very different (Figure 18). While the main phases within the transfer functions can be seen in both seismograms, the short-period transfer function

contains far more amplitude variation. This is due to the short-period seismometer's bandwidth at higher frequencies. The velocity inversion results of the two methods share both similarities and differences (Figure 18). The upper ~10 km of the short-period velocity profile agrees with the upper ~10 km of the broadband profile. The rest of the short-period velocity profile follows the overall trend of the broadband profile, but displays far more variation and detail. Thus the short-period seismometer transfer function study is much more detailed than that of a broadband seismometer transfer function study and may provide a more detailed velocity model due to its higher frequency bandwidth.

The uppermost 10 km within the ETSZ shows erratic velocity contrasts beginning at lower velocities and increasing up to ~6 km/s at 10 km depth. This does not correlate with the large horizontal decollement as the decollement is 0-5 km deep in our study area. Station TVNC shows a high velocity layer at shallow depths. This could be related to the igneous rocks that are present at the surface within the Blue Ridge province. More studies will need to be performed to learn more about the upper 10 km within the ETSZ.

A striking feature visible in several of the velocity profiles is the presence of a high velocity layer at ~60-65 km depth (Figure 17; Figure 19b). This is noteworthy because it agrees well with findings from Langston (1994) for station CCM (Cathedral Cave, Missouri) showing a high velocity layer 10 -15 km thick within the mantle around 60 km depth with P-wave velocity of 8.5 km/s. Our mantle high velocity layer, where visible, has P-wave velocities ranging from ~8.2-8.58 km/s. These velocities are comparable to velocities for rock compositions of mafic eclogite or ultramafic dunite (Christensen, 1996). The depth to the top of the high velocity zone in our study varies

from west to east (Figure 19b). Stations RCGA, DYTN, BCRT, and TZTN are associated with a prominent high velocity layer around 60 km depth. For stations GMG, ETT, CPCT, CCRT, and GRBT, the high velocity layer is located around 65 km. It is noteworthy that the change in depth to the top of the high velocity layer occurs across the vertical projection of the NY-AL magnetic lineament.

Past tectonics of the region may be better explained by the presence of the high velocity mantle feature found in our study. The high velocity zone has a 5 km down-step to the east within the ETSZ across the NY-AL lineament. This change in structure within the ETSZ may suggest that the NY-AL lineament is a large basement fault that affects the entire crust and part of the upper mantle. Langston (1994) finds a high velocity zone in Missouri at 60 km depth. This observation combined with our results suggests that the upper mantle high velocity zone could be present over a very broad area. Basement rocks in Missouri are within the Granite Rhyolite province, and the upper mantle high velocity zone could represent preserved ultramafic rocks associated with its formation. If this high velocity zone is associated with the Granite Rhyolite province, it is a good assumption that the Granite Rhyolite rocks could extend into our study area. This would imply that Grenville basement rocks were thrust over Granite Rhyolite basement during a past continental collision.

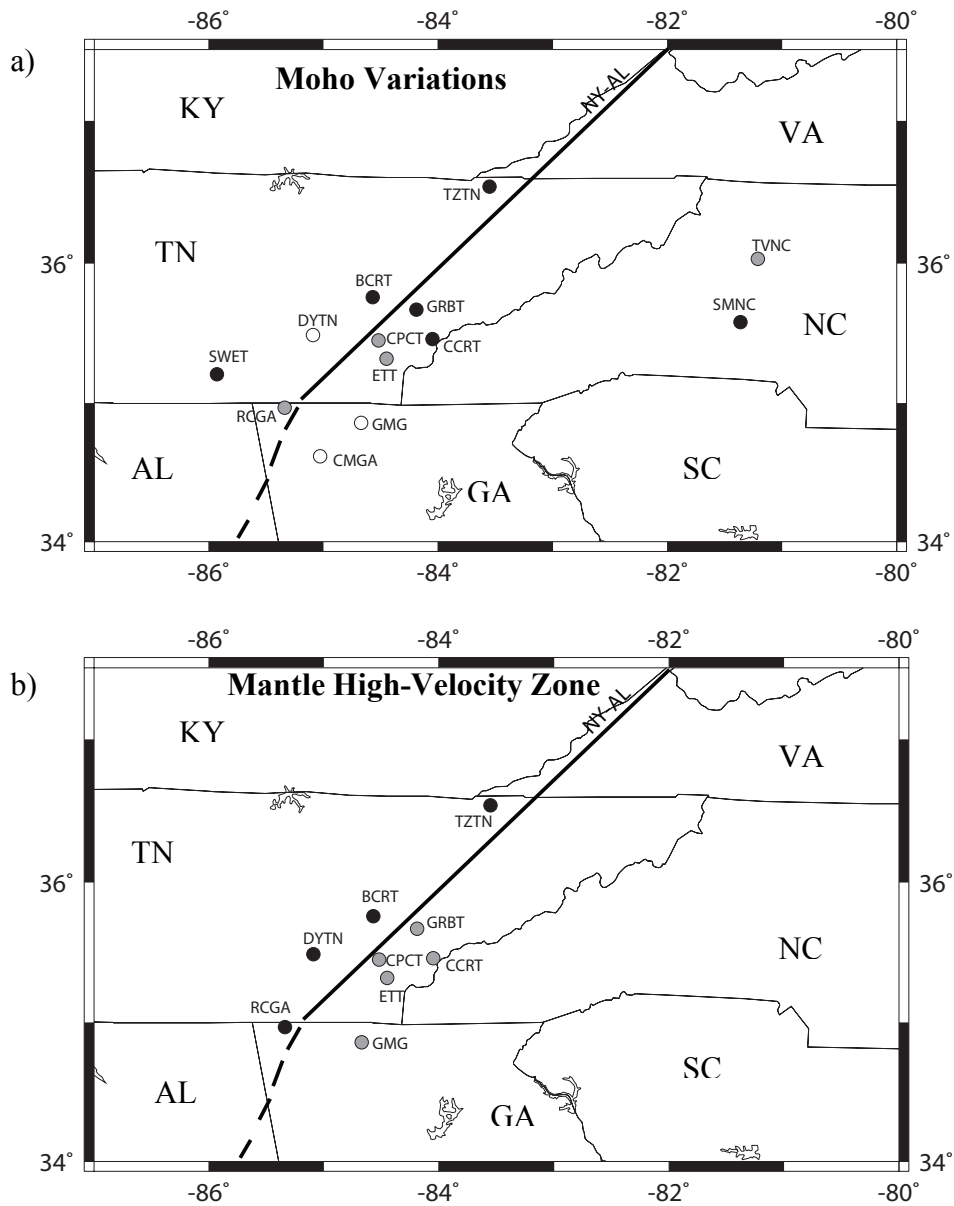


Figure 19: Maps depicting some of the various boundaries found in the inversion results. a) Map where Moho discontinuities can be seen. Black is a station where the Moho can be clearly seen on the velocity profile. The Moho is generally around 46-48 km depth within the ETSZ. Gray is a station where the Moho is somewhat noticeable. Clear circles are stations where the Moho is gradational and does not show any sharp discontinuities. b) Locations where the 60-65 km upper mantle high velocity zone can be seen. Black is a 60 km depth high velocity zone, and gray is a 65 km depth high velocity zone. Notice the abrupt drop from 60 to 65 km across the NY-AL lineament.

CONCLUSIONS

We have demonstrated that a short-period seismometer array works very well for radial component transfer function studies. The higher frequency bandwidth allows for better retention of amplitude variations through the deconvolution process. This, in turn, results in acceptable inversion results for velocity versus depth. We have shown the complexity and uniqueness of the ETSZ through our methods.

Moho depth in our area of study does not vary much in any particular direction. It is mainly located around 45-50 km depth. However, some of our stations within the ETSZ show a laminated Moho boundary adding to the complexity of our study area.

The presence of a high velocity layer in the upper mantle at 60-65 km depth is intriguing and sparks curiosity about its origin. This layer is seen in other studies to the west of our research area, and we believe it extends into our area. The 5 km down-step across the NY-AL lineament opens for discussion the assumption that the NY-AL lineament is a deeper structure than previously thought and affects not only the upper crust, but the lower crust and upper mantle as well.

Further studies can be performed using the Earthscope transportable array (TA) and the FlexArray network associated with the Northern Embayment Lithosphere Experiment (NELE) (Langston, 2011). Gaps or other changes in the upper mantle high velocity zone could place constraints on past rifting cycles including the Reelfoot rift in the NMSZ.

REFERENCES

- Ammon, C. J., Randall, G. E., and Zandt, G., 1990, On the nonuniqueness of receiver function inversions: *Journal of Geophysical Research*, v. 95, p. 15303-15318.
- Baker, M. S., 2006, Investigation of the crust and uppermost mantle in the Carolina Terrane and Blue Ridge, Southern Appalachians, using receiver function analysis of broadband earthquake data [M.S. Thesis]: Athens, University of Georgia, 104 p.
- Bartholomew, M. J. and Hatcher, R. D., 2010, The Grenville orogenic cycle of southern Laurentia: Unraveling sutures, rifts, and shear zones as potential piercing points for Amazonia: *Journal of South American Earth Sciences*, v. 29, p. 4-20.
- Brocher, T. M., 2005, Empirical relations between elastic wavespeeds and density in the Earth's crust: *Bulletin of the Seismological Society of America*, v. 95, p. 2081-2092.
- Chapman, M. C., Powell, C. A., Vlahovic, G., and Sibol, M. S., 1997, A statistical analysis of earthquake focal mechanisms and epicenter locations in the Eastern Tennessee Seismic Zone: *Bulletin of the Seismological Society of America*, v. 87, p. 1522-1536.
- Christensen, N. I., 1996, Poisson's ratio and crustal seismology: *Journal of Geophysical Research*, v. 101, p. 3139-3156.
- Constable, S. C., Parker, R. L., and Constable, C. G., 1987, Occam's inversion: A practical algorithm for generating smooth models from electromagnetic sounding data: *Geophysics*, v. 52, p. 289-300.
- Cook, F. A. and Vasudevan, K., 2006, Reprocessing and enhanced interpretation of the initial COCORP Southern Appalachian traverse: *Tectonophysics*, v. 420, p. 161-174.
- Culotta, R. C., Pratt, T., and Oliver, J., 1990, A tale of two sutures: COCORP's deep seismic surveys of the Grenville province in the eastern U.S. midcontinent: *Geology*, v. 18, p. 646-649.
- Fisher, C. M., Loewy, S. L., Miller, C. F., Berquist, P., Van Schmus, W. R., Hatcher, R. D., Wooden, J. L., and Fullagar, P. D., 2010, Whole-rock Pb and Sm-Nd isotopic constraints on the growth of southeastern Laurentia during Grenvillian orogenesis: *GSA Bulletin*, v. 122, p. 1646-1659.

- Hale, D. H., Thompson, G. A., 1982, The seismic reflection character of the continental Mohorovicic discontinuity: *Journal of Geophysical Research*, v. 87, p. 4625-4635.
- Hawman, R. B., 2008, Crustal thickness variations across the Blue Ridge Mountains, Southern Appalachians: An alternative procedure for migrating wide-angle reflection data: *Bulletin of the Seismological Society of America*, v. 98, p. 469-475.
- Hopkins, D. L., 1995, The New York – Alabama magnetic lineament: Its reflection character and relationship to the Grenville Front [Ph.D. Dissertation]: Blacksburg, Virginia Polytechnic Institute and State University, 176 p.
- Johnston, A. C., and Kanter, L. R., 1990, Earthquakes in stable continental crust: *Scientific American*, v. 262, p. 68-75.
- Jones, C. H., and Phinney, R. A., 1998, Seismic structure of the lithosphere from teleseismic converted arrivals observed at small arrays in the southern Sierra Nevada and vicinity, California: *Journal of Geophysical Research*, v. 103, p. 10065-10090.
- Keller, G. R., Bland, A. E., and Greenberg, J. K., 1982, Evidence for a major Late Precambrian tectonic event (rifting?) in the Eastern Midcontinent Region, United States: *Tectonics*, v. 1, p. 213-223.
- King, E. R., and Zietz, I., 1978, The New York – Alabama lineament: Geophysical evidence for a major crustal break in the basement beneath the Appalachian basin: *Geology*, v. 6, p. 312-318.
- Langston, C. A., 1977a, Corvallis, Oregon, crustal and upper mantle receiver structure from teleseismic P and S waves: *Bulletin of the Seismological Society of America*, v. 67, p. 713-724.
- Langston, C. A., 1977b, The effect of planar dipping structure on source and receiver responses for constant ray parameter: *Bulletin of the Seismological Society of America*, v. 67, p. 1029-1050.
- Langston, C. A., 1979, Structure under Mount Rainier, Washington, inferred from teleseismic body waves: *Journal of Geophysical Research*, v. 84, p. 4749-4762.
- Langston, C. A., 1981, Evidence for the subducting lithosphere under southern Vancouver Island and western Oregon from teleseismic P wave conversions: *Journal of Geophysical Research*, v. 86, p. 3857-3866.
- Langston, C. A., 1989, Scattering of teleseismic body waves under Pasadena, California: *Journal of Geophysical Research*, v. 94, p. 1935-1951.

- Meissner, R., 1973, The 'Moho' as a transition zone: *Surveys in Geophysics*, v. 1, p. 195-216.
- Langston, C. A., 1994, An integrated study of crustal structure and regional wave propagation for southeastern Missouri: *Bulletin of the Seismological Society of America*, v. 84, p. 105-118.
- Langston, C. A., and Hammer, J. K., 2001, The vertical component P-wave receiver function: *Bulletin of the Seismological Society of America*, v. 91, p. 1805-1819.
- Langston, C. A., 2011, Northern Embayment Lithosphere Experiment: <http://www.ceri.memphis.edu/NELE/index.html>.
- Owens, T. J., Zandt, G., and Taylor, S. R., 1984, Seismic evidence for an ancient rift beneath the Cumberland Plateau, Tennessee: A detailed analysis of broadband teleseismic P waveforms: *Journal of Geophysical Research*, v. 89, p. 7783-7795.
- Owens, T. J., Taylor, S. R., and Zandt, G., 1987, Crustal structure at regional seismic test network stations determined from inversion of broadband teleseismic P waveforms: *Bulletin of the Seismological Society of America*, v. 77, p. 631-662.
- Powell, C. A., Bollinger, G. A., Chapman, M. C., Sibol, M. S., Johnston, A. C., and Wheeler, R. L., 1994, A seismotectonic model for the 300-kilometer-long Eastern Tennessee Seismic Zone: *Science*, v. 264, p. 686-688.
- Powell, C., Withers, M., Vlahovic, G., Arroucau, P., and Cox, R., 2012, Three-Dimensional P- and S-wave velocity models for the Eastern Tennessee Seismic Zone: *Journal of Geophysical Research*, *submitted*.
- Steltenpohl, M. G., Zietz, I., Horton, J. W., and Daniels, D. L., 2010, New York Alabama lineament: A buried right-slip fault bordering the Appalachians and mid continent North America: *Geology*, v. 38, p. 571-574.
- Thomas, W. A., 2006, Tectonic inheritance at a continental margin: *GSA Today*, v. 16, p. 4-11.
- Vlahovic, G., Powell, C. A., Chapman, M. C., and Sibol, M. S., 1998, Joint hypocenter velocity inversion for the eastern Tennessee seismic zone: *Journal of Geophysical Research*, v. 103, p. 4879-4896.
- Wagner, L. S., Metcalf, K., and Stewart, K., 2010, Lower crustal and mantle lithospheric structure of the North Carolina Blue Ridge Mountains and Piedmont: *Geology*, *submitted*.

APPENDIX A

Table 4: Table showing the list of events used in this study.

Date	Time	Latitude, °	Longitude, °	Depth, km	M_W
14 April 2004	01 hr 54 min 09 sec	55.19 N	162.65 E	51.3	6.2
03 May 2004	04 hr 36 min 52 sec	37.61 S	73.27 W	33.2	6.6
15 June 2004	11 hr 16 min 31 sec	38.84 S	73.10 W	37.9	6.1
12 November 2004	06 hr 36 min 15 sec	26.65 S	63.22 W	553.0	6.1
21 March 2005	12 hr 23 min 52 sec	24.68 S	63.43 W	561.6	6.9
21 March 2005	12 hr 43 min 11 sec	24.93 S	63.36 W	557.8	6.4
13 June 2005	22 hr 33 min 33 sec	19.90 S	69.12 W	108.4	7.8
14 June 2005	17 hr 10 min 17 sec	51.31 N	179.41 E	51.7	6.8
09 September 2005	11 hr 26 min 03 sec	31.64 S	69.00 W	86.2	6.0
26 September 2005	01 hr 55 min 39 sec	5.61 S	76.37 W	132.3	7.5
17 November 2005	19 hr 26 min 56 sec	22.26 S	67.78 W	162.5	6.9
08 January 2006	11 hr 34 min 53 sec	36.20 N	23.44 E	48.4	6.6
20 April 2006	23 hr 25 min 05 sec	61.09 N	167.10 E	43.0	7.7
10 May 2006	02 hr 42 min 54 sec	52.61 N	169.22 W	43.0	6.4
22 May 2006	13 hr 08 min 02 sec	54.32 N	158.43 E	189.4	6.2
17 August 2006	11 hr 11 min 38 sec	55.68 N	161.66 E	84.9	6.2
24 August 2006	21 hr 50 min 39 sec	51.19 N	157.52 E	70.1	6.4
25 August 2006	00 hr 44 min 43 sec	24.32 S	66.89 W	156.8	6.4
17 September 2006	09 hr 34 min 09 sec	31.67 S	67.00 W	105.2	6.2
22 September 2006	02 hr 32 min 26 sec	26.74 S	63.02 W	598.5	6.0
29 September 2006	13 hr 08 min 25 sec	10.91 N	61.65 W	53.0	6.1
30 September 2006	16 hr 26 min 56 sec	15.52 S	73.05 W	106.7	6.0
15 October 2006	17 hr 07 min 49 sec	19.88 N	155.93 W	38.9	6.6
20 October 2006	10 hr 48 min 57 sec	13.44 S	76.58 W	32.2	6.7
21 April 2007	17 hr 53 min 46 sec	45.27 S	72.60 W	44.1	6.2
29 April 2007	12 hr 41 min 58 sec	52.04 N	179.97 W	125.3	6.2
30 May 2007	20 hr 22 min 12 sec	52.14 N	157.31 E	115.8	6.4
13 July 2007	21 hr 54 min 43 sec	51.81 N	176.23 W	35.0	6.0
15 August 2007	23 hr 40 min 56 sec	13.36 S	76.52 W	30.2	8.0
18 August 2007	02 hr 52 min 36 sec	13.78 S	76.23 W	39.2	6.0
03 September 2007	16 hr 14 min 54 sec	45.83 N	150.03 E	99.6	6.2
14 November 2007	15 hr 40 min 53 sec	22.19 S	69.84 W	60.0	7.7
16 December 2007	08 hr 09 min 18 sec	22.93 S	70.08 W	52.6	6.6
21 December 2007	07 hr 24 min 36 sec	51.42 N	179.08 W	35.0	6.1
29 December 2007	22 hr 58 min 06 sec	52.62 N	168.37 W	35.0	6.0
15 February 2008	14 hr 45 min 11 sec	21.23 S	68.01 W	134.3	6.0
16 April 2008	05 hr 54 min 23 sec	51.95 N	179.12 W	31.5	6.5
05 July 2008	02 hr 12 min 04 sec	53.89 N	152.88 E	633.3	7.7

Table 4 cont.: Table showing the list of events used in this study.

Date	Time	Latitude, °	Longitude, °	Depth, km	M_W
08 July 2008	09 hr 13 min 02 sec	15.96 S	71.68 W	74.3	6.0
15 July 2008	03 hr 26 min 36 sec	35.98 N	27.79 E	68.4	6.4
03 September 2008	11 hr 25 min 14 sec	26.72 S	63.20 W	569.9	6.3
11 September 2008	00 hr 20 min 52 sec	41.98 N	143.63 E	35.0	6.9
12 October 2008	20 hr 55 min 42 sec	20.02 S	64.94 W	356.0	6.2
24 November 2008	09 hr 02 min 58 sec	54.18 N	154.31 E	487.5	7.0
15 January 2009	17 hr 49 min 39 sec	46.86 N	155.16 E	36.0	7.4
15 February 2009	10 hr 04 min 51 sec	5.84 S	80.88 W	35.6	6.2
18 April 2009	19 hr 17 min 59 sec	46.12 N	151.36 E	35.0	6.6
12 July 2009	19 hr 11 min 45 sec	14.99 S	70.42 W	201.6	6.1
27 February 2010	07 hr 37 min 18 sec	34.75 S	72.39 W	35.0	6.0
27 February 2010	06 hr 34 min 14 sec	35.85 S	72.72 W	35.0	8.8
24 May 2010	16 hr 18 min 29 sec	8.07 S	71.57 W	580.5	6.5
12 August 2010	11 hr 54 min 16 sec	1.26 S	77.31 W	211.0	7.1
01 January 2011	09 hr 56 min 59 sec	26.76 S	63.10 W	583.6	7.0

APPENDIX B

Table 5: Inversion values corresponding to results from Figure 12 for station BCRT. Velocities are in km/s, density in g/cc, and thickness is in km.

V_P			V_S			ρ			<i>thickness</i>
Average	Max	Min	Average	Max	Min	Average	Max	Min	
3.9179	4.0632	3.8610	2.2647	2.3487	2.2318	2.4480	2.4704	2.4391	1.0000
4.1611	4.2506	4.1018	2.4053	2.4570	2.3710	2.4851	2.4984	2.4762	1.0000
4.7546	4.7865	4.7021	2.7483	2.7668	2.7180	2.5694	2.5737	2.5623	1.0000
4.6670	4.7297	4.5400	2.6977	2.7339	2.6243	2.5574	2.5660	2.5399	1.0000
5.3014	5.3684	5.2289	3.0644	3.1031	3.0225	2.6403	2.6486	2.6312	1.0000
5.6096	5.7646	5.4787	3.2425	3.3322	3.1669	2.6778	2.6961	2.6621	1.0000
5.7168	5.8140	5.5784	3.3045	3.3607	3.2245	2.6905	2.7019	2.6741	2.0000
6.2929	6.4742	6.0315	3.6375	3.7423	3.4864	2.7558	2.7755	2.7268	2.0000
6.8421	7.2216	6.3766	3.9550	4.1744	3.6859	2.8137	2.8524	2.7650	2.0000
6.9202	7.2203	6.4767	4.0001	4.1736	3.7437	2.8218	2.8523	2.7758	2.0000
7.0359	7.4619	6.5014	4.0670	4.3132	3.7580	2.8333	2.8758	2.7784	2.0000
6.9970	7.3543	6.5741	4.0445	4.2511	3.8000	2.8296	2.8654	2.7862	3.0000
6.8309	7.0248	6.6068	3.9485	4.0606	3.8189	2.8129	2.8327	2.7896	3.0000
6.6234	6.7022	6.5338	3.8286	3.8741	3.7768	2.7914	2.7996	2.7819	3.0000
6.7192	6.8295	6.6429	3.8839	3.9477	3.8398	2.8014	2.8129	2.7934	3.0000
6.7325	6.9943	6.5703	3.8916	4.0429	3.7979	2.8027	2.8297	2.7858	3.0000
6.9212	7.0419	6.7636	4.0007	4.0705	3.9096	2.8222	2.8345	2.8060	3.0000
6.8487	7.0987	6.6002	3.9588	4.1033	3.8152	2.8147	2.8402	2.7889	3.0000
6.9596	7.2411	6.7229	4.0229	4.1856	3.8861	2.8260	2.8543	2.8018	3.0000
6.9737	7.2602	6.6786	4.0310	4.1967	3.8604	2.8274	2.8562	2.7972	3.0000
7.0095	7.3475	6.5279	4.0517	4.2471	3.7734	2.8308	2.8647	2.7813	3.0000
7.0738	7.3345	6.6415	4.0889	4.2396	3.8390	2.8374	2.8635	2.7933	3.0000
7.5629	7.7220	7.3312	4.3716	4.4636	4.2377	2.8854	2.9006	2.8631	3.0000
7.8012	8.0535	7.4247	4.5093	4.6552	4.2917	2.9077	2.9312	2.8722	3.0000
8.1497	8.5746	7.7026	4.7108	4.9564	4.4524	2.9397	2.9775	2.8987	3.0000
8.4589	9.0337	7.7844	4.8895	5.2218	4.4997	2.9669	3.0166	2.9064	2.0000
8.3124	8.8257	7.6568	4.8049	5.1016	4.4259	2.9539	2.9991	2.8944	2.0000
8.1176	8.5659	7.5604	4.6923	4.9514	4.3702	2.9366	2.9768	2.8853	2.0000
8.1074	8.6781	7.4920	4.6863	5.0163	4.3307	2.9356	2.9865	2.8787	2.0000
8.0717	8.6185	7.4560	4.6657	4.9818	4.3098	2.9323	2.9813	2.8752	2.0000
8.0951	8.5458	7.5874	4.6793	4.9398	4.3858	2.9346	2.9750	2.8878	2.0000
8.2711	8.7278	7.7189	4.7810	5.0450	4.4618	2.9505	2.9907	2.9003	2.0000
8.3574	8.9353	7.6875	4.8309	5.1649	4.4437	2.9579	3.0083	2.8973	2.0000
8.2945	8.8825	7.6009	4.7945	5.1344	4.3936	2.9522	3.0039	2.8891	2.0000
8.2690	8.9659	7.5651	4.7797	5.1826	4.3729	2.9500	3.0109	2.8857	2.0000
8.1965	8.8527	7.5253	4.7378	5.1172	4.3499	2.9434	3.0014	2.8819	2.0000

Table 6: Inversion values corresponding to results from Figure 12 for station CCRT. Velocities are in km/s, density in g/cc, and thickness is in km.

V_P			V_S			ρ			<i>thickness</i>
Average	Max	Min	Average	Max	Min	Average	Max	Min	
4.3844	4.4637	4.2940	2.5343	2.5801	2.4821	2.5178	2.5291	2.5048	1.0000
4.5674	4.6621	4.5398	2.6401	2.6948	2.6242	2.5437	2.5568	2.5399	1.0000
4.6544	4.7147	4.5549	2.6904	2.7253	2.6329	2.5557	2.5640	2.5420	1.0000
4.5498	4.6238	4.3978	2.6299	2.6727	2.5421	2.5412	2.5515	2.5198	1.0000
5.0899	5.1318	4.9931	2.9421	2.9663	2.8862	2.6135	2.6189	2.6010	1.0000
5.4234	5.4547	5.3680	3.1349	3.1530	3.1029	2.6553	2.6591	2.6485	1.0000
6.0023	6.0666	5.9377	3.4695	3.5067	3.4322	2.7235	2.7308	2.7161	2.0000
6.2860	6.3912	6.2130	3.6335	3.6944	3.5913	2.7551	2.7666	2.7471	2.0000
6.2626	6.2882	6.2089	3.6200	3.6348	3.5890	2.7526	2.7554	2.7467	2.0000
6.5394	6.5934	6.4650	3.7800	3.8112	3.7370	2.7825	2.7882	2.7745	2.0000
6.7193	6.8369	6.6279	3.8840	3.9520	3.8312	2.8014	2.8136	2.7919	2.0000
6.6430	6.7150	6.5858	3.8399	3.8815	3.8068	2.7934	2.8010	2.7874	3.0000
7.0921	7.2979	6.9726	4.0995	4.2184	4.0304	2.8395	2.8599	2.8275	3.0000
7.2092	7.3554	7.1028	4.1671	4.2517	4.1057	2.8511	2.8655	2.8406	3.0000
7.2663	7.4985	7.1264	4.2002	4.3344	4.1193	2.8567	2.8793	2.8429	3.0000
7.4012	7.6219	7.2350	4.2782	4.4057	4.1821	2.8699	2.8911	2.8537	3.0000
7.6486	7.8455	7.5239	4.4211	4.5350	4.3491	2.8936	2.9121	2.8818	3.0000
7.3804	7.4952	7.2354	4.2661	4.3325	4.1823	2.8679	2.8790	2.8537	3.0000
7.5270	7.7324	7.3134	4.3509	4.4696	4.2274	2.8820	2.9015	2.8614	3.0000
7.3258	7.4888	7.0860	4.2346	4.3288	4.0959	2.8625	2.8784	2.8389	3.0000
7.3354	7.4379	7.2017	4.2401	4.2994	4.1629	2.8635	2.8735	2.8504	3.0000
7.7284	7.8320	7.6030	4.4673	4.5272	4.3948	2.9011	2.9108	2.8893	3.0000
7.9370	8.0756	7.7987	4.5879	4.6680	4.5079	2.9205	2.9332	2.9077	3.0000
8.0313	8.2362	7.8866	4.6424	4.7608	4.5587	2.9291	2.9477	2.9159	3.0000
7.9998	8.2503	7.8346	4.6242	4.7690	4.5287	2.9262	2.9489	2.9111	3.0000
7.8396	8.0176	7.6613	4.5315	4.6345	4.4285	2.9115	2.9279	2.8948	2.0000
7.6985	7.9207	7.3503	4.4500	4.5785	4.2487	2.8982	2.9190	2.8650	2.0000
7.9092	8.1987	7.4307	4.5718	4.7391	4.2952	2.9178	2.9443	2.8728	2.0000
8.2009	8.5434	7.8062	4.7404	4.9384	4.5123	2.9444	2.9748	2.9084	2.0000
8.1423	8.5228	7.6780	4.7065	4.9265	4.4381	2.9391	2.9730	2.8964	2.0000
7.9779	8.3667	7.3733	4.6115	4.8362	4.2620	2.9240	2.9593	2.8672	2.0000
8.0675	8.4361	7.5951	4.6633	4.8763	4.3902	2.9323	2.9654	2.8886	2.0000
8.0978	8.4755	7.6328	4.6808	4.8992	4.4120	2.9350	2.9689	2.8921	2.0000
7.9369	8.3120	7.3819	4.5878	4.8046	4.2670	2.9203	2.9544	2.8681	2.0000
7.8489	8.2037	7.3106	4.5369	4.7420	4.2258	2.9121	2.9448	2.8611	2.0000
7.9220	8.2747	7.4093	4.5792	4.7831	4.2829	2.9189	2.9511	2.8707	2.0000

Table 7: Inversion values corresponding to results from Figure 12 for station CMGA. Velocities are in km/s, density in g/cc, and thickness is in km.

V_P			V_S			ρ			<i>thickness</i>
Average	Max	Min	Average	Max	Min	Average	Max	Min	
3.7462	3.8413	3.5322	2.1654	2.2204	2.0417	2.4205	2.4360	2.3854	1.0000
4.4289	4.6130	4.3426	2.5601	2.6665	2.5101	2.5241	2.5500	2.5118	1.0000
5.2731	5.3276	5.1724	3.0480	3.0795	2.9898	2.6367	2.6435	2.6240	1.0000
5.5296	5.5714	5.4723	3.1963	3.2204	3.1632	2.6682	2.6732	2.6613	1.0000
5.8204	5.9587	5.7523	3.3644	3.4443	3.3250	2.7026	2.7185	2.6947	1.0000
5.7704	5.8068	5.6953	3.3355	3.3565	3.2921	2.6968	2.7011	2.6880	1.0000
5.8145	5.9074	5.6266	3.3610	3.4147	3.2524	2.7019	2.7127	2.6798	2.0000
5.9941	6.1985	5.7954	3.4648	3.5830	3.3499	2.7225	2.7455	2.6997	2.0000
6.4995	6.7708	6.3704	3.7570	3.9138	3.6823	2.7781	2.8068	2.7643	2.0000
6.6889	6.9584	6.4970	3.8664	4.0222	3.7555	2.7981	2.8260	2.7780	2.0000
6.5808	6.7814	6.4151	3.8039	3.9199	3.7081	2.7868	2.8079	2.7692	2.0000
6.5420	6.7341	6.3426	3.7815	3.8925	3.6663	2.7827	2.8030	2.7613	3.0000
6.6767	6.8811	6.4473	3.8593	3.9775	3.7268	2.7969	2.8181	2.7726	3.0000
6.7456	6.9950	6.5253	3.8992	4.0433	3.7718	2.8040	2.8297	2.7810	3.0000
6.8989	7.2288	6.7100	3.9878	4.1785	3.8786	2.8197	2.8531	2.8005	3.0000
7.0162	7.2184	6.8854	4.0556	4.1725	3.9800	2.8318	2.8521	2.8186	3.0000
7.1023	7.2798	7.0090	4.1054	4.2080	4.0515	2.8405	2.8581	2.8312	3.0000
7.1855	7.2586	6.9962	4.1535	4.1957	4.0441	2.8488	2.8560	2.8299	3.0000
7.4145	7.5415	7.1698	4.2859	4.3593	4.1444	2.8712	2.8835	2.8473	3.0000
7.3896	7.4966	7.2114	4.2714	4.3333	4.1684	2.8688	2.8792	2.8514	3.0000
7.2414	7.4364	6.9386	4.1858	4.2985	4.0108	2.8542	2.8734	2.8240	3.0000
7.4469	7.6015	7.1688	4.3045	4.3939	4.1438	2.8743	2.8892	2.8472	3.0000
7.5584	7.6870	7.3214	4.3690	4.4434	4.2320	2.8850	2.8973	2.8622	3.0000
7.3666	7.5612	7.0101	4.2582	4.3706	4.0521	2.8664	2.8853	2.8313	3.0000
7.8130	8.0939	7.5191	4.5162	4.6786	4.3463	2.9089	2.9349	2.8813	3.0000
8.0947	8.3439	7.8688	4.6790	4.8231	4.5484	2.9348	2.9573	2.9142	2.0000
8.0997	8.3783	7.7866	4.6819	4.8429	4.5009	2.9352	2.9603	2.9066	2.0000
8.1285	8.4364	7.8534	4.6986	4.8766	4.5395	2.9378	2.9654	2.9128	2.0000
8.1230	8.4497	7.8442	4.6954	4.8842	4.5342	2.9373	2.9666	2.9120	2.0000
8.0681	8.3751	7.7924	4.6636	4.8411	4.5043	2.9323	2.9600	2.9071	2.0000
8.0660	8.4070	7.7633	4.6624	4.8595	4.4875	2.9321	2.9628	2.9044	2.0000
8.2781	8.6444	7.9900	4.7851	4.9968	4.6185	2.9512	2.9836	2.9254	2.0000
8.3880	8.7868	8.0449	4.8486	5.0791	4.6502	2.9609	2.9958	2.9304	2.0000
8.2621	8.6843	7.9138	4.7758	5.0198	4.5744	2.9497	2.9870	2.9184	2.0000
8.0604	8.5644	7.5821	4.6592	4.9505	4.3827	2.9314	2.9766	2.8873	2.0000
8.0966	8.5824	7.7329	4.6801	4.9609	4.4699	2.9348	2.9782	2.9016	2.0000

Table 8: Inversion values corresponding to results from Figure 12 for station CPCT. Velocities are in km/s, density in g/cc, and thickness is in km.

V_P			V_S			ρ			<i>thickness</i>
Average	Max	Min	Average	Max	Min	Average	Max	Min	
3.9984	4.1863	3.8532	2.3112	2.4198	2.2273	2.4603	2.4889	2.4378	1.0000
4.2375	4.3262	4.1910	2.4494	2.5007	2.4225	2.4964	2.5094	2.4896	1.0000
4.4085	4.4999	4.3200	2.5483	2.6011	2.4971	2.5212	2.5342	2.5085	1.0000
4.9743	5.0045	4.9345	2.8753	2.8928	2.8523	2.5986	2.6025	2.5933	1.0000
5.2871	5.3244	5.2479	3.0561	3.0777	3.0335	2.6385	2.6431	2.6336	1.0000
5.7208	5.8061	5.6275	3.3068	3.3561	3.2529	2.6910	2.7010	2.6800	1.0000
6.0892	6.1786	5.9777	3.5198	3.5715	3.4553	2.7333	2.7433	2.7207	2.0000
6.1655	6.2538	6.0569	3.5639	3.6149	3.5011	2.7418	2.7516	2.7297	2.0000
6.4656	6.5917	6.3222	3.7373	3.8103	3.6544	2.7746	2.7880	2.7591	2.0000
6.7930	6.9745	6.5830	3.9266	4.0315	3.8052	2.8090	2.8277	2.7871	2.0000
6.8816	6.9745	6.7518	3.9778	4.0315	3.9028	2.8182	2.8277	2.8048	2.0000
7.0443	7.1588	6.9054	4.0719	4.1380	3.9916	2.8347	2.8462	2.8206	3.0000
6.9177	6.9871	6.8532	3.9987	4.0388	3.9614	2.8219	2.8289	2.8153	3.0000
6.9723	7.0603	6.9032	4.0302	4.0811	3.9903	2.8274	2.8363	2.8204	3.0000
7.0478	7.1516	6.9825	4.0739	4.1339	4.0361	2.8350	2.8454	2.8285	3.0000
7.1473	7.2325	7.0678	4.1314	4.1807	4.0854	2.8450	2.8535	2.8371	3.0000
7.2074	7.3054	7.0913	4.1661	4.2228	4.0990	2.8510	2.8606	2.8394	3.0000
7.4754	7.6484	7.2890	4.3210	4.4210	4.2133	2.8771	2.8936	2.8590	3.0000
7.3585	7.5202	7.1530	4.2534	4.3469	4.1347	2.8657	2.8814	2.8456	3.0000
7.2960	7.4776	7.0842	4.2173	4.3223	4.0949	2.8596	2.8773	2.8387	3.0000
7.3830	7.5948	7.1588	4.2676	4.3900	4.1380	2.8681	2.8885	2.8462	3.0000
7.5844	7.8099	7.3388	4.3840	4.5144	4.2421	2.8875	2.9088	2.8639	3.0000
7.7967	8.0477	7.4912	4.5068	4.6518	4.3301	2.9074	2.9307	2.8786	3.0000
7.8532	8.1395	7.5596	4.5394	4.7049	4.3697	2.9127	2.9390	2.8852	3.0000
7.9151	8.2264	7.6026	4.5752	4.7551	4.3945	2.9184	2.9468	2.8893	3.0000
7.9188	8.2426	7.6111	4.5773	4.7645	4.3995	2.9187	2.9483	2.8901	2.0000
7.9494	8.2702	7.6363	4.5950	4.7805	4.4140	2.9215	2.9507	2.8925	2.0000
7.9651	8.3027	7.6591	4.6041	4.7992	4.4272	2.9229	2.9536	2.8946	2.0000
7.9527	8.3295	7.6412	4.5969	4.8148	4.4169	2.9218	2.9560	2.8929	2.0000
7.8547	8.2926	7.5123	4.5403	4.7934	4.3424	2.9127	2.9527	2.8807	2.0000
7.6834	8.1632	7.2616	4.4413	4.7186	4.1975	2.8966	2.9411	2.8563	2.0000
7.5760	8.0330	7.1191	4.3792	4.6434	4.1151	2.8865	2.9293	2.8422	2.0000
7.6209	8.0247	7.2159	4.4051	4.6386	4.1710	2.8908	2.9286	2.8518	2.0000
7.6704	8.0892	7.2805	4.4338	4.6758	4.2084	2.8955	2.9344	2.8582	2.0000
7.6482	8.1025	7.2273	4.4209	4.6835	4.1776	2.8934	2.9356	2.8529	2.0000
7.7573	8.1474	7.4323	4.4840	4.7095	4.2961	2.9037	2.9397	2.8730	2.0000

Table 9: Inversion values corresponding to results from Figure 12 for station DYTN. Velocities are in km/s, density in g/cc, and thickness is in km.

V_P			V_S			ρ			<i>thickness</i>
Average	Max	Min	Average	Max	Min	Average	Max	Min	
3.4557	3.5275	3.3216	1.9975	2.0390	1.9200	2.3723	2.3846	2.3490	1.0000
4.0240	4.0938	3.9783	2.3260	2.3664	2.2996	2.4644	2.4750	2.4574	1.0000
5.1893	5.2763	5.1553	2.9995	3.0499	2.9800	2.6262	2.6371	2.6219	1.0000
4.9784	5.0694	4.8684	2.8777	2.9303	2.8141	2.5991	2.6109	2.5846	1.0000
5.3601	5.5226	5.2876	3.0983	3.1923	3.0564	2.6475	2.6674	2.6385	1.0000
5.6241	5.6792	5.5661	3.2509	3.2828	3.2174	2.6795	2.6861	2.6726	1.0000
5.5904	5.7344	5.4696	3.2315	3.3147	3.1616	2.6755	2.6926	2.6610	2.0000
5.6682	5.7941	5.5213	3.2764	3.3492	3.1915	2.6847	2.6996	2.6672	2.0000
6.4308	6.5577	6.3349	3.7172	3.7906	3.6618	2.7708	2.7844	2.7605	2.0000
6.8458	6.9653	6.7407	3.9571	4.0262	3.8964	2.8145	2.8267	2.8037	2.0000
6.7980	6.9597	6.6504	3.9295	4.0229	3.8442	2.8095	2.8262	2.7942	2.0000
6.7520	6.8643	6.6691	3.9029	3.9678	3.8550	2.8048	2.8164	2.7962	3.0000
6.8348	6.9543	6.7681	3.9507	4.0198	3.9122	2.8134	2.8256	2.8065	3.0000
6.4087	6.4823	6.3317	3.7044	3.7470	3.6599	2.7685	2.7764	2.7601	3.0000
6.9415	7.0520	6.8698	4.0125	4.0763	3.9710	2.8243	2.8355	2.8170	3.0000
6.8984	7.1321	6.7163	3.9875	4.1226	3.8823	2.8198	2.8435	2.8011	3.0000
6.7650	7.0110	6.5173	3.9105	4.0526	3.7673	2.8061	2.8314	2.7801	3.0000
6.9059	7.1091	6.5105	3.9918	4.1093	3.7633	2.8204	2.8412	2.7794	3.0000
6.9537	7.1906	6.4655	4.0195	4.1564	3.7373	2.8252	2.8493	2.7746	3.0000
7.2024	7.4476	6.6625	4.1632	4.3049	3.8511	2.8501	2.8744	2.7955	3.0000
6.9297	7.2223	6.1902	4.0056	4.1747	3.5782	2.8224	2.8525	2.7446	3.0000
6.8715	7.1615	6.2850	3.9720	4.1396	3.6330	2.8167	2.8464	2.7550	3.0000
7.1538	7.5491	6.4490	4.1351	4.3637	3.7277	2.8450	2.8842	2.7728	3.0000
7.1972	7.6148	6.6185	4.1602	4.4016	3.8257	2.8494	2.8904	2.7909	3.0000
7.7486	8.1940	7.1526	4.4789	4.7364	4.1344	2.9025	2.9439	2.8455	3.0000
7.9092	8.4147	7.2424	4.5718	4.8640	4.1864	2.9173	2.9635	2.8544	2.0000
8.0470	8.6048	7.3621	4.6514	4.9739	4.2555	2.9299	2.9801	2.8662	2.0000
8.0605	8.7504	7.2164	4.6593	5.0580	4.1713	2.9307	2.9926	2.8519	2.0000
7.9886	8.7291	7.1160	4.6177	5.0457	4.1133	2.9241	2.9908	2.8419	2.0000
7.9566	8.6210	7.2657	4.5992	4.9833	4.1998	2.9215	2.9815	2.8567	2.0000
8.0548	8.6457	7.4233	4.6559	4.9975	4.2909	2.9306	2.9837	2.8721	2.0000
8.1508	8.7760	7.4149	4.7114	5.0728	4.2860	2.9391	2.9948	2.8713	2.0000
8.1704	8.8492	7.4647	4.7228	5.1151	4.3149	2.9409	3.0011	2.8761	2.0000
8.2011	8.8373	7.6473	4.7405	5.1083	4.4204	2.9438	3.0001	2.8935	2.0000
8.3149	8.9898	7.6017	4.8063	5.1964	4.3940	2.9538	3.0129	2.8892	2.0000
8.3109	9.1407	7.3864	4.8040	5.2837	4.2696	2.9528	3.0255	2.8685	2.0000

Table 10: Inversion values corresponding to results from Figure 12 for station ETT. Velocities are in km/s, density in g/cc, and thickness is in km.

V_P			V_S			ρ			<i>thickness</i>
Average	Max	Min	Average	Max	Min	Average	Max	Min	
3.5000	3.5555	3.3560	2.0231	2.0552	1.9399	2.3799	2.3893	2.3551	1.0000
4.3530	4.7544	4.1375	2.5162	2.7482	2.3916	2.5128	2.5694	2.4816	1.0000
4.1757	4.2834	3.9103	2.4137	2.4759	2.2603	2.4871	2.5032	2.4468	1.0000
4.5701	4.7176	4.3534	2.6417	2.7269	2.5164	2.5439	2.5644	2.5134	1.0000
5.2142	5.3616	4.9598	3.0140	3.0992	2.8669	2.6292	2.6477	2.5967	1.0000
5.8670	6.0761	5.4181	3.3913	3.5122	3.1318	2.7076	2.7318	2.6547	1.0000
6.2048	6.4453	5.7353	3.5866	3.7256	3.3152	2.7457	2.7724	2.6927	2.0000
5.9671	6.1957	5.4915	3.4492	3.5813	3.1743	2.7191	2.7452	2.6636	2.0000
6.3980	6.5574	6.2818	3.6982	3.7904	3.6311	2.7673	2.7844	2.7547	2.0000
6.6111	6.8777	6.0604	3.8214	3.9755	3.5031	2.7896	2.8178	2.7301	2.0000
6.5553	6.8559	5.9724	3.7892	3.9630	3.4523	2.7835	2.8156	2.7201	2.0000
6.6813	6.9296	6.2046	3.8620	4.0056	3.5865	2.7970	2.8231	2.7462	3.0000
6.6186	6.8879	6.1211	3.8258	3.9815	3.5382	2.7905	2.8188	2.7369	3.0000
6.7397	6.9666	6.4533	3.8958	4.0270	3.7302	2.8034	2.8269	2.7733	3.0000
6.8190	7.0347	6.5896	3.9416	4.0663	3.8090	2.8117	2.8337	2.7878	3.0000
6.9379	7.1838	6.6314	4.0104	4.1525	3.8332	2.8238	2.8486	2.7922	3.0000
7.1546	7.4388	6.8861	4.1356	4.2999	3.9804	2.8456	2.8736	2.8187	3.0000
7.1220	7.4556	6.7711	4.1168	4.3096	3.9139	2.8423	2.8752	2.8068	3.0000
7.5243	7.9916	7.1083	4.3493	4.6194	4.1088	2.8815	2.9255	2.8411	3.0000
7.7681	8.1829	7.3094	4.4902	4.7300	4.2251	2.9045	2.9429	2.8610	3.0000
7.3494	7.8360	6.8503	4.2482	4.5295	3.9597	2.8643	2.9112	2.8150	3.0000
7.4057	7.6739	6.9655	4.2808	4.4358	4.0263	2.8701	2.8960	2.8268	3.0000
7.8223	8.1930	7.2790	4.5215	4.7358	4.2075	2.9096	2.9438	2.8580	3.0000
7.8037	8.2774	7.0782	4.5108	4.7846	4.0914	2.9077	2.9514	2.8381	3.0000
7.6856	8.2959	7.0441	4.4425	4.7953	4.0717	2.8967	2.9530	2.8347	3.0000
7.9508	8.3768	7.5206	4.5958	4.8421	4.3472	2.9215	2.9602	2.8815	2.0000
8.2064	8.6528	7.6113	4.7436	5.0016	4.3996	2.9446	2.9843	2.8901	2.0000
8.2630	8.9027	7.4684	4.7763	5.1461	4.3170	2.9494	3.0056	2.8764	2.0000
8.2766	9.1565	7.4875	4.7841	5.2927	4.3281	2.9505	3.0268	2.8783	2.0000
8.2108	9.0221	7.3214	4.7461	5.2151	4.2320	2.9447	3.0156	2.8622	2.0000
7.9698	8.6818	7.1725	4.6068	5.0184	4.1459	2.9229	2.9868	2.8475	2.0000
7.8942	8.4655	7.4089	4.5632	4.8934	4.2826	2.9163	2.9680	2.8707	2.0000
8.0658	8.5747	7.6058	4.6624	4.9565	4.3964	2.9320	2.9775	2.8896	2.0000
8.1794	8.6659	7.5726	4.7279	5.0092	4.3772	2.9422	2.9854	2.8864	2.0000
8.1495	8.5521	7.5887	4.7107	4.9434	4.3865	2.9396	2.9756	2.8880	2.0000
8.1764	8.5767	7.6744	4.7262	4.9576	4.4361	2.9420	2.9777	2.8961	2.0000

Table 11: Inversion values corresponding to results from Figure 12 for station GMG. Velocities are in km/s, density in g/cc, and thickness is in km.

V_P			V_S			ρ			<i>thickness</i>
Average	Max	Min	Average	Max	Min	Average	Max	Min	
4.3352	5.1231	3.9720	2.5059	2.9613	2.2960	2.5097	2.6178	2.4564	1.0000
4.6725	5.1594	4.5400	2.7009	2.9823	2.6243	2.5579	2.6224	2.5399	1.0000
4.7846	5.0765	4.6556	2.7656	2.9344	2.6911	2.5733	2.6118	2.5559	1.0000
4.9512	5.0930	4.8338	2.8620	2.9439	2.7941	2.5955	2.6139	2.5800	1.0000
5.3173	5.5205	5.2092	3.0736	3.1910	3.0111	2.6422	2.6671	2.6287	1.0000
5.5918	5.6459	5.5432	3.2322	3.2635	3.2041	2.6757	2.6821	2.6699	1.0000
5.6721	5.7451	5.5663	3.2787	3.3209	3.2175	2.6852	2.6938	2.6726	2.0000
5.8187	6.0016	5.5469	3.3634	3.4691	3.2063	2.7023	2.7234	2.6703	2.0000
5.9721	6.0910	5.7188	3.4521	3.5208	3.3057	2.7200	2.7335	2.6908	2.0000
5.9674	6.0832	5.6515	3.4493	3.5163	3.2667	2.7194	2.7326	2.6828	2.0000
6.3132	6.4185	6.0615	3.6493	3.7101	3.5038	2.7580	2.7695	2.7302	2.0000
6.9055	7.1072	6.5625	3.9916	4.1082	3.7934	2.8205	2.8410	2.7849	3.0000
6.7798	6.9155	6.5927	3.9189	3.9974	3.8108	2.8077	2.8217	2.7881	3.0000
6.8674	7.0226	6.6846	3.9696	4.0593	3.8639	2.8167	2.8325	2.7978	3.0000
6.9710	7.1092	6.7375	4.0295	4.1093	3.8945	2.8272	2.8412	2.8033	3.0000
7.1799	7.3726	6.9291	4.1502	4.2616	4.0053	2.8482	2.8672	2.8230	3.0000
7.2346	7.4589	6.8686	4.1818	4.3115	3.9703	2.8536	2.8755	2.8169	3.0000
7.3956	7.6206	7.0520	4.2749	4.4050	4.0763	2.8693	2.8910	2.8355	3.0000
7.3961	7.5799	7.0287	4.2752	4.3815	4.0629	2.8694	2.8871	2.8331	3.0000
7.4467	7.6475	7.1224	4.3044	4.4205	4.1170	2.8743	2.8935	2.8425	3.0000
7.6505	7.8133	7.2777	4.4222	4.5163	4.2068	2.8937	2.9091	2.8579	3.0000
7.7798	7.9526	7.4144	4.4970	4.5969	4.2858	2.9059	2.9220	2.8712	3.0000
7.9061	8.1034	7.3913	4.5700	4.6841	4.2724	2.9175	2.9357	2.8690	3.0000
7.8312	8.0365	7.3746	4.5267	4.6454	4.2628	2.9106	2.9296	2.8674	3.0000
7.8658	8.0467	7.5104	4.5467	4.6513	4.3413	2.9139	2.9306	2.8805	3.0000
7.9864	8.2259	7.4340	4.6164	4.7549	4.2971	2.9249	2.9468	2.8731	2.0000
7.9133	8.1784	7.4007	4.5742	4.7274	4.2779	2.9181	2.9425	2.8699	2.0000
7.8427	8.0507	7.6371	4.5334	4.6536	4.4145	2.9117	2.9309	2.8926	2.0000
8.0605	8.2176	7.7973	4.6593	4.7501	4.5071	2.9317	2.9460	2.9076	2.0000
8.2521	8.4886	7.6970	4.7700	4.9067	4.4491	2.9489	2.9700	2.8982	2.0000
8.1367	8.4654	7.5856	4.7033	4.8933	4.3847	2.9385	2.9680	2.8877	2.0000
7.9856	8.3297	7.5474	4.6160	4.8149	4.3627	2.9247	2.9560	2.8840	2.0000
7.9471	8.2700	7.5254	4.5937	4.7803	4.3499	2.9212	2.9507	2.8819	2.0000
7.9435	8.2535	7.5001	4.5916	4.7708	4.3353	2.9208	2.9492	2.8795	2.0000
7.9361	8.2676	7.4493	4.5873	4.7790	4.3059	2.9201	2.9505	2.8746	2.0000
7.8979	8.2441	7.4011	4.5653	4.7653	4.2781	2.9165	2.9484	2.8699	2.0000

Table 12: Inversion values corresponding to results from Figure 12 for station GRBT. Velocities are in km/s, density in g/cc, and thickness is in km.

V_P			V_S			ρ			<i>thickness</i>
Average	Max	Min	Average	Max	Min	Average	Max	Min	
4.8270	5.0067	4.4379	2.7902	2.8941	2.5653	2.5789	2.6028	2.5255	1.0000
4.8834	5.0252	4.5968	2.8228	2.9047	2.6571	2.5865	2.6052	2.5478	1.0000
5.1354	5.2119	5.0271	2.9684	3.0126	2.9059	2.6193	2.6290	2.6054	1.0000
5.0198	5.1069	4.9074	2.9017	2.9520	2.8367	2.6044	2.6157	2.5898	1.0000
5.4160	5.4616	5.2529	3.1306	3.1570	3.0363	2.6544	2.6600	2.6342	1.0000
5.6041	5.6540	5.5437	3.2394	3.2682	3.2044	2.6772	2.6831	2.6699	1.0000
6.0209	6.1713	5.9106	3.4803	3.5672	3.4166	2.7256	2.7425	2.7131	2.0000
6.2601	6.3430	6.1611	3.6186	3.6665	3.5613	2.7523	2.7614	2.7413	2.0000
6.2568	6.3593	6.1804	3.6166	3.6759	3.5725	2.7519	2.7631	2.7435	2.0000
6.3514	6.4554	6.2720	3.6713	3.7314	3.6254	2.7623	2.7735	2.7536	2.0000
6.3403	6.3944	6.2944	3.6649	3.6962	3.6384	2.7611	2.7669	2.7561	2.0000
6.5148	6.7460	6.4449	3.7658	3.8994	3.7253	2.7798	2.8042	2.7724	3.0000
6.6109	6.7039	6.5320	3.8214	3.8751	3.7757	2.7901	2.7998	2.7817	3.0000
6.5817	6.6834	6.4660	3.8045	3.8633	3.7376	2.7869	2.7977	2.7746	3.0000
6.5937	6.7407	6.4059	3.8114	3.8964	3.7028	2.7882	2.8037	2.7682	3.0000
6.9734	7.0518	6.8883	4.0309	4.0762	3.9816	2.8275	2.8355	2.8189	3.0000
7.2214	7.2818	7.1479	4.1742	4.2091	4.1317	2.8523	2.8583	2.8451	3.0000
7.1186	7.2360	7.0187	4.1148	4.1827	4.0571	2.8421	2.8538	2.8321	3.0000
7.1119	7.2844	6.9383	4.1109	4.2106	4.0106	2.8414	2.8586	2.8240	3.0000
7.1246	7.3286	6.9143	4.1183	4.2362	3.9967	2.8427	2.8629	2.8215	3.0000
7.1424	7.3884	6.8893	4.1286	4.2707	3.9823	2.8444	2.8687	2.8190	3.0000
7.4498	7.6144	7.2768	4.3062	4.4014	4.2062	2.8746	2.8904	2.8578	3.0000
7.7632	8.0447	7.5930	4.4874	4.6501	4.3890	2.9044	2.9304	2.8884	3.0000
7.9605	8.2945	7.7660	4.6015	4.7945	4.4890	2.9226	2.9529	2.9047	3.0000
8.0033	8.3742	7.7515	4.6262	4.8406	4.4806	2.9265	2.9600	2.9033	3.0000
8.0462	8.3462	7.8083	4.6510	4.8244	4.5135	2.9304	2.9575	2.9086	2.0000
8.1912	8.5412	7.9231	4.7348	4.9371	4.5798	2.9435	2.9746	2.9193	2.0000
8.3098	8.7391	7.9679	4.8033	5.0515	4.6057	2.9540	2.9917	2.9234	2.0000
8.2600	8.6556	7.9081	4.7746	5.0032	4.5711	2.9496	2.9845	2.9179	2.0000
8.1231	8.3905	7.8245	4.6954	4.8500	4.5228	2.9373	2.9614	2.9101	2.0000
8.0497	8.2928	7.7741	4.6530	4.7935	4.4937	2.9307	2.9527	2.9054	2.0000
8.0321	8.2793	7.7477	4.6428	4.7857	4.4784	2.9291	2.9515	2.9030	2.0000
8.0073	8.2699	7.7473	4.6285	4.7803	4.4782	2.9268	2.9507	2.9029	2.0000
7.9871	8.2700	7.7617	4.6168	4.7803	4.4865	2.9250	2.9507	2.9043	2.0000
8.0153	8.2848	7.7670	4.6331	4.7889	4.4896	2.9276	2.9520	2.9048	2.0000
8.0988	8.3257	7.8278	4.6814	4.8125	4.5247	2.9352	2.9557	2.9104	2.0000

Table 13: Inversion values corresponding to results from Figure 12 for station RCGA. Velocities are in km/s, density in g/cc, and thickness is in km.

V_P			V_S			ρ			<i>thickness</i>
Average	Max	Min	Average	Max	Min	Average	Max	Min	
3.6579	3.8799	3.4475	2.1144	2.2427	1.9928	2.4061	2.4420	2.3710	1.0000
4.2615	4.6617	4.0552	2.4633	2.6946	2.3440	2.4996	2.5567	2.4692	1.0000
5.3748	5.5551	5.2081	3.1068	3.2110	3.0104	2.6493	2.6713	2.6286	1.0000
4.8783	4.9762	4.7816	2.8198	2.8764	2.7639	2.5859	2.5988	2.5730	1.0000
5.2370	5.3773	4.9876	3.0271	3.1083	2.8830	2.6321	2.6497	2.6003	1.0000
5.4977	5.7411	5.2278	3.1779	3.3186	3.0218	2.6641	2.6934	2.6310	1.0000
5.2472	5.4241	4.9623	3.0331	3.1353	2.8684	2.6333	2.6554	2.5970	2.0000
5.7647	5.9399	5.6054	3.3322	3.4335	3.2401	2.6961	2.7164	2.6773	2.0000
6.6879	7.2139	6.2735	3.8658	4.1699	3.6263	2.7976	2.8516	2.7538	2.0000
6.8361	7.5313	6.3768	3.9515	4.3533	3.6860	2.8127	2.8825	2.7650	2.0000
6.4492	6.8210	6.0886	3.7279	3.9428	3.5194	2.7726	2.8120	2.7332	2.0000
7.0641	7.3537	6.7441	4.0833	4.2507	3.8983	2.8365	2.8653	2.8040	3.0000
6.5970	6.7882	6.1688	3.8133	3.9238	3.5658	2.7885	2.8086	2.7422	3.0000
6.9985	7.2034	6.6100	4.0454	4.1638	3.8208	2.8300	2.8506	2.7900	3.0000
6.9707	7.3804	6.5379	4.0293	4.2661	3.7791	2.8271	2.8679	2.7823	3.0000
7.2643	7.6895	6.6971	4.1990	4.4448	3.8712	2.8562	2.8975	2.7991	3.0000
7.4565	7.8768	6.9181	4.3102	4.5531	3.9989	2.8750	2.9150	2.8219	3.0000
7.2266	8.0463	6.5411	4.1773	4.6511	3.7810	2.8523	2.9305	2.7827	3.0000
6.7052	7.5817	6.0736	3.8758	4.3825	3.5107	2.7983	2.8873	2.7316	3.0000
6.6194	7.6645	5.8741	3.8262	4.4303	3.3954	2.7885	2.8951	2.7088	3.0000
6.2899	7.4347	5.3043	3.6358	4.2975	3.0661	2.7520	2.8732	2.6406	3.0000
6.4463	7.1597	5.5730	3.7262	4.1385	3.2214	2.7701	2.8462	2.6734	3.0000
7.1923	7.7193	6.6208	4.1574	4.4620	3.8271	2.8487	2.9003	2.7911	3.0000
7.2250	8.1208	6.5143	4.1763	4.6941	3.7655	2.8511	2.9373	2.7798	3.0000
7.9112	8.4375	7.4762	4.5730	4.8772	4.3215	2.9179	2.9655	2.8772	3.0000
8.2807	9.0792	7.7688	4.7865	5.2481	4.4907	2.9511	3.0204	2.9049	2.0000
8.3001	8.9790	7.7556	4.7977	5.1902	4.4830	2.9529	3.0120	2.9037	2.0000
8.1886	8.5321	7.4567	4.7333	4.9318	4.3102	2.9430	2.9738	2.8753	2.0000
8.0141	8.3764	7.0431	4.6324	4.8418	4.0712	2.9270	2.9601	2.8346	2.0000
7.8168	8.2225	6.9346	4.5184	4.7529	4.0084	2.9089	2.9465	2.8236	2.0000
7.7033	8.1401	7.0398	4.4527	4.7053	4.0692	2.8983	2.9390	2.8343	2.0000
7.7984	8.1257	7.2278	4.5078	4.6970	4.1779	2.9074	2.9378	2.8530	2.0000
7.9747	8.6004	7.4138	4.6097	4.9713	4.2854	2.9233	2.9797	2.8712	2.0000
8.1075	8.7767	7.4985	4.6864	5.0733	4.3344	2.9354	2.9949	2.8793	2.0000
8.2378	8.9149	7.7328	4.7617	5.1531	4.4698	2.9472	3.0066	2.9016	2.0000
8.2909	8.8508	7.8390	4.7924	5.1160	4.5312	2.9522	3.0012	2.9115	2.0000

Table 14: Inversion values corresponding to results from Figure 12 for station SMNC. Velocities are in km/s, density in g/cc, and thickness is in km.

V_P			V_S			ρ			<i>thickness</i>
Average	Max	Min	Average	Max	Min	Average	Max	Min	
3.6770	3.8085	3.3819	2.1254	2.2015	1.9549	2.4093	2.4307	2.3596	1.0000
5.0719	5.2535	4.9518	2.9317	3.0367	2.8623	2.6111	2.6343	2.5956	1.0000
5.4283	5.8562	5.2572	3.1377	3.3851	3.0388	2.6557	2.7068	2.6347	1.0000
5.9423	6.0803	5.7047	3.4348	3.5146	3.2975	2.7166	2.7323	2.6891	1.0000
5.8197	6.0357	5.6949	3.3639	3.4888	3.2918	2.7025	2.7273	2.6879	1.0000
5.9317	5.9803	5.8170	3.4287	3.4568	3.3624	2.7154	2.7210	2.7022	1.0000
6.2612	6.4103	6.1528	3.6192	3.7054	3.5565	2.7524	2.7687	2.7404	2.0000
6.0173	6.1305	5.8885	3.4782	3.5437	3.4038	2.7252	2.7379	2.7105	2.0000
6.3652	6.6447	6.2107	3.6793	3.8409	3.5900	2.7637	2.7936	2.7468	2.0000
6.2673	6.4136	6.0630	3.6227	3.7073	3.5046	2.7530	2.7690	2.7304	2.0000
6.6302	6.8196	6.4052	3.8325	3.9420	3.7024	2.7920	2.8118	2.7681	2.0000
6.9503	7.0734	6.7591	4.0175	4.0887	3.9070	2.8251	2.8376	2.8056	3.0000
7.3838	7.6375	7.0999	4.2681	4.4147	4.1040	2.8681	2.8926	2.8403	3.0000
6.9506	7.1671	6.7443	4.0177	4.1428	3.8985	2.8252	2.8470	2.8040	3.0000
6.9248	7.1100	6.6453	4.0028	4.1098	3.8412	2.8225	2.8413	2.7937	3.0000
6.8151	7.0012	6.4601	3.9393	4.0469	3.7341	2.8112	2.8304	2.7740	3.0000
7.0940	7.2807	6.9853	4.1006	4.2085	4.0377	2.8397	2.8582	2.8288	3.0000
6.9001	7.0862	6.7533	3.9885	4.0961	3.9037	2.8200	2.8389	2.8050	3.0000
7.1793	7.4823	7.0104	4.1499	4.3250	4.0522	2.8481	2.8778	2.8313	3.0000
6.8741	7.1346	6.6770	3.9735	4.1240	3.8595	2.8173	2.8437	2.7970	3.0000
6.5983	6.9101	6.2797	3.8141	3.9943	3.6299	2.7885	2.8211	2.7544	3.0000
7.4492	7.8558	7.1578	4.3059	4.5409	4.1375	2.8744	2.9130	2.8461	3.0000
7.9256	8.2699	7.5465	4.5813	4.7803	4.3621	2.9193	2.9507	2.8839	3.0000
8.0446	8.8170	7.5487	4.6501	5.0965	4.3634	2.9299	2.9983	2.8841	3.0000
7.2523	7.7952	6.8733	4.1921	4.5059	3.9730	2.8550	2.9074	2.8174	3.0000
7.3156	7.6559	7.0112	4.2287	4.4254	4.0527	2.8613	2.8943	2.8314	2.0000
7.7688	8.1385	7.4733	4.4907	4.7043	4.3198	2.9048	2.9389	2.8769	2.0000
8.3006	8.6474	7.8806	4.7981	4.9985	4.5553	2.9532	2.9838	2.9153	2.0000
8.2665	8.6975	7.7984	4.7783	5.0274	4.5077	2.9501	2.9881	2.9077	2.0000
7.9997	8.5300	7.6499	4.6241	4.9306	4.4219	2.9261	2.9736	2.8938	2.0000
8.1863	8.5806	7.6446	4.7320	4.9599	4.4188	2.9430	2.9780	2.8933	2.0000
8.6608	9.0623	8.2124	5.0063	5.2383	4.7471	2.9847	3.0190	2.9456	2.0000
8.4196	9.2001	7.6694	4.8669	5.3180	4.4332	2.9633	3.0304	2.8956	2.0000
7.7220	8.4730	7.1925	4.4636	4.8977	4.1575	2.9000	2.9686	2.8495	2.0000
8.0420	8.4177	7.7034	4.6485	4.8657	4.4528	2.9299	2.9638	2.8988	2.0000
8.4712	8.8280	8.0396	4.8966	5.1029	4.6472	2.9682	2.9993	2.9299	2.0000

Table 15: Inversion values corresponding to results from Figure 12 for station SWET. Velocities are in km/s, density in g/cc, and thickness is in km.

V_P			V_S			ρ			<i>thickness</i>
Average	Max	Min	Average	Max	Min	Average	Max	Min	
4.5307	4.9193	4.1328	2.6189	2.8435	2.3889	2.5373	2.5913	2.4809	1.0000
4.7347	4.8124	4.6345	2.7368	2.7817	2.6789	2.5667	2.5772	2.5530	1.0000
6.0268	6.3133	5.8492	3.4837	3.6493	3.3811	2.7262	2.7581	2.7060	1.0000
5.5517	5.6302	5.4525	3.2091	3.2544	3.1517	2.6709	2.6803	2.6589	1.0000
5.7020	5.7822	5.5885	3.2959	3.3423	3.2304	2.6888	2.6982	2.6753	1.0000
5.2532	5.4721	5.0914	3.0365	3.1631	2.9430	2.6341	2.6613	2.6137	1.0000
5.6232	5.8895	5.4108	3.2504	3.4043	3.1276	2.6792	2.7106	2.6538	2.0000
6.4677	6.7135	6.2452	3.7385	3.8806	3.6099	2.7746	2.8008	2.7507	2.0000
6.6347	6.7711	6.5466	3.8351	3.9139	3.7841	2.7925	2.8068	2.7833	2.0000
6.2264	6.3086	6.1512	3.5991	3.6466	3.5556	2.7486	2.7576	2.7402	2.0000
6.3361	6.5276	6.0808	3.6625	3.7732	3.5149	2.7605	2.7812	2.7324	2.0000
6.2236	6.3370	6.0435	3.5975	3.6630	3.4933	2.7482	2.7607	2.7282	3.0000
6.3222	6.4147	6.2006	3.6544	3.7079	3.5841	2.7591	2.7691	2.7457	3.0000
6.3984	6.4951	6.2002	3.6985	3.7544	3.5839	2.7673	2.7778	2.7457	3.0000
6.6727	6.7466	6.4913	3.8571	3.8998	3.7522	2.7965	2.8043	2.7774	3.0000
6.8911	7.0762	6.7391	3.9833	4.0903	3.8954	2.8191	2.8379	2.8035	3.0000
7.0657	7.2260	6.8851	4.0843	4.1769	3.9798	2.8368	2.8528	2.8186	3.0000
6.9576	7.0779	6.6981	4.0217	4.0912	3.8717	2.8259	2.8381	2.7992	3.0000
7.0904	7.2370	6.8131	4.0985	4.1832	3.9382	2.8393	2.8539	2.8112	3.0000
7.3368	7.7001	7.0526	4.2409	4.4509	4.0766	2.8635	2.8985	2.8355	3.0000
7.7317	8.1327	7.4768	4.4692	4.7010	4.3218	2.9013	2.9384	2.8773	3.0000
8.0772	8.6447	7.7144	4.6689	4.9969	4.4592	2.9330	2.9836	2.8998	3.0000
8.0059	8.4678	7.6929	4.6277	4.8947	4.4468	2.9266	2.9682	2.8978	3.0000
7.9310	8.1924	7.6993	4.5844	4.7355	4.4505	2.9199	2.9438	2.8984	3.0000
7.8765	8.0932	7.6255	4.5529	4.6781	4.4078	2.9149	2.9348	2.8915	3.0000
7.6691	7.9591	7.3878	4.4330	4.6007	4.2704	2.8955	2.9226	2.8687	2.0000
7.6948	8.0506	7.2605	4.4479	4.6536	4.1968	2.8979	2.9309	2.8562	2.0000
7.9008	8.2862	7.4937	4.5669	4.7897	4.3316	2.9171	2.9521	2.8789	2.0000
8.0399	8.4418	7.6907	4.6473	4.8796	4.4455	2.9298	2.9659	2.8976	2.0000
8.0083	8.4198	7.6187	4.6291	4.8669	4.4039	2.9269	2.9640	2.8908	2.0000
7.8811	8.3074	7.3991	4.5556	4.8020	4.2769	2.9152	2.9540	2.8698	2.0000
7.8180	8.2725	7.2612	4.5191	4.7818	4.1973	2.9092	2.9509	2.8563	2.0000
7.9032	8.3901	7.2903	4.5683	4.8498	4.2140	2.9170	2.9614	2.8591	2.0000
8.1096	8.6021	7.5019	4.6876	4.9723	4.3364	2.9360	2.9799	2.8797	2.0000
8.3310	8.7886	7.7395	4.8156	5.0801	4.4737	2.9559	2.9959	2.9022	2.0000
8.4200	8.8530	7.8299	4.8671	5.1174	4.5259	2.9637	3.0014	2.9106	2.0000

Table 16: Inversion values corresponding to results from Figure 12 for station TVNC. Velocities are in km/s, density in g/cc, and thickness is in km.

V_P			V_S			ρ			<i>thickness</i>
Average	Max	Min	Average	Max	Min	Average	Max	Min	
5.0366	5.2870	4.8223	2.9113	3.0561	2.7875	2.6065	2.6385	2.5785	1.0000
3.9864	4.0677	3.8983	2.3043	2.3513	2.2534	2.4586	2.4711	2.4449	1.0000
4.5045	4.5775	4.3943	2.6037	2.6460	2.5400	2.5348	2.5451	2.5192	1.0000
5.2353	5.3755	5.1320	3.0262	3.1072	2.9665	2.6319	2.6494	2.6189	1.0000
6.0422	6.1139	5.9974	3.4926	3.5340	3.4667	2.7280	2.7361	2.7230	1.0000
6.2876	6.3648	6.1546	3.6344	3.6791	3.5576	2.7553	2.7637	2.7406	1.0000
6.3810	6.4357	6.2732	3.6884	3.7201	3.6261	2.7655	2.7714	2.7537	2.0000
6.0112	6.1085	5.9003	3.4747	3.5309	3.4106	2.7245	2.7355	2.7119	2.0000
7.0320	7.2306	6.9331	4.0647	4.1795	4.0076	2.8334	2.8533	2.8235	2.0000
6.9903	7.0706	6.9354	4.0406	4.0870	4.0089	2.8292	2.8373	2.8237	2.0000
7.3296	7.5272	7.1805	4.2367	4.3510	4.1505	2.8629	2.8821	2.8483	2.0000
7.3670	7.5637	7.2030	4.2584	4.3721	4.1636	2.8666	2.8856	2.8505	3.0000
7.0914	7.2075	6.9912	4.0991	4.1662	4.0411	2.8394	2.8510	2.8293	3.0000
6.8469	6.9409	6.7851	3.9577	4.0121	3.9220	2.8146	2.8242	2.8083	3.0000
6.6956	6.7790	6.6546	3.8703	3.9185	3.8466	2.7989	2.8076	2.7947	3.0000
6.7702	6.8434	6.7253	3.9134	3.9557	3.8875	2.8067	2.8143	2.8021	3.0000
6.7627	6.7969	6.7377	3.9090	3.9288	3.8946	2.8059	2.8095	2.8033	3.0000
6.8502	6.8887	6.7632	3.9596	3.9819	3.9094	2.8150	2.8189	2.8060	3.0000
7.4558	7.5214	7.3832	4.3097	4.3476	4.2677	2.8752	2.8815	2.8682	3.0000
7.8149	8.2205	7.5528	4.5173	4.7517	4.3658	2.9091	2.9463	2.8845	3.0000
6.6282	6.8407	6.1539	3.8314	3.9542	3.5572	2.7917	2.8140	2.7405	3.0000
7.3776	7.6337	6.9540	4.2645	4.4126	4.0197	2.8675	2.8922	2.8256	3.0000
7.0100	7.2867	6.7684	4.0520	4.2120	3.9124	2.8311	2.8588	2.8065	3.0000
7.2385	7.5141	7.0778	4.1841	4.3434	4.0912	2.8540	2.8808	2.8381	3.0000
7.3280	7.5920	7.1261	4.2359	4.3884	4.1192	2.8627	2.8883	2.8429	3.0000
7.5352	7.7132	7.3453	4.3556	4.4585	4.2459	2.8828	2.8997	2.8645	2.0000
7.5875	7.9414	7.3914	4.3858	4.5904	4.2725	2.8877	2.9209	2.8690	2.0000
7.6926	7.8865	7.4798	4.4466	4.5586	4.3236	2.8977	2.9159	2.8775	2.0000
8.0437	8.3032	7.8589	4.6496	4.7995	4.5427	2.9302	2.9537	2.9133	2.0000
8.0325	8.4704	7.7578	4.6430	4.8962	4.4843	2.9291	2.9684	2.9039	2.0000
7.6551	8.2810	7.1894	4.4249	4.7867	4.1557	2.8938	2.9517	2.8492	2.0000
7.9249	8.1105	7.6496	4.5809	4.6882	4.4217	2.9193	2.9364	2.8937	2.0000
8.1572	8.6440	7.8626	4.7151	4.9965	4.5448	2.9403	2.9835	2.9137	2.0000
8.1713	8.5796	7.8343	4.7233	4.9593	4.5285	2.9416	2.9779	2.9110	2.0000
8.2724	8.5917	7.9384	4.7817	4.9663	4.5887	2.9507	2.9790	2.9207	2.0000
8.3366	8.7480	7.9455	4.8188	5.0566	4.5928	2.9564	2.9924	2.9213	2.0000

Table 17: Inversion values corresponding to results from Figure 12 for station TZTN. Velocities are in km/s, density in g/cc, and thickness is in km.

V_P			V_S			ρ			<i>thickness</i>
Average	Max	Min	Average	Max	Min	Average	Max	Min	
4.3754	4.7882	4.1627	2.5291	2.7677	2.4062	2.5160	2.5739	2.4854	1.0000
4.6645	4.9809	4.4421	2.6962	2.8791	2.5677	2.5567	2.5994	2.5261	1.0000
5.4480	5.8221	5.1157	3.1492	3.3654	2.9571	2.6579	2.7028	2.6168	1.0000
4.5379	4.6285	4.4439	2.6230	2.6754	2.5687	2.5395	2.5522	2.5263	1.0000
5.4137	5.5367	5.2722	3.1293	3.2004	3.0475	2.6541	2.6691	2.6366	1.0000
5.7490	5.8678	5.5769	3.3231	3.3918	3.2237	2.6942	2.7081	2.6739	1.0000
5.9963	6.1985	5.8539	3.4661	3.5830	3.3838	2.7227	2.7455	2.7065	2.0000
6.3648	6.6227	6.1762	3.6791	3.8282	3.5700	2.7636	2.7913	2.7430	2.0000
5.9875	6.0762	5.7635	3.4610	3.5122	3.3315	2.7217	2.7318	2.6960	2.0000
5.7376	5.8925	5.5149	3.3165	3.4060	3.1878	2.6929	2.7110	2.6665	2.0000
6.0713	6.2660	5.7530	3.5094	3.6219	3.3254	2.7311	2.7529	2.6948	2.0000
6.7487	6.9805	6.3294	3.9010	4.0350	3.6586	2.8043	2.8283	2.7599	3.0000
6.5785	6.8468	6.2950	3.8026	3.9577	3.6387	2.7864	2.8146	2.7561	3.0000
6.5482	6.8541	6.2972	3.7850	3.9619	3.6400	2.7832	2.8154	2.7564	3.0000
6.4864	6.8662	6.1713	3.7494	3.9689	3.5673	2.7765	2.8166	2.7425	3.0000
6.6623	7.0200	6.3768	3.8511	4.0578	3.6860	2.7952	2.8323	2.7650	3.0000
6.7565	7.1581	6.3635	3.9055	4.1377	3.6783	2.8049	2.8461	2.7636	3.0000
6.5739	7.1320	6.1046	3.7999	4.1225	3.5287	2.7854	2.8435	2.7350	3.0000
6.8206	7.2408	6.3397	3.9426	4.1855	3.6646	2.8114	2.8543	2.7610	3.0000
6.9730	7.3691	6.4861	4.0306	4.2596	3.7492	2.8270	2.8668	2.7768	3.0000
7.1711	7.4495	6.6675	4.1451	4.3061	3.8541	2.8470	2.8746	2.7960	3.0000
7.6106	8.0082	7.1324	4.3992	4.6290	4.1228	2.8897	2.9271	2.8435	3.0000
7.9794	8.3889	7.5053	4.6124	4.8491	4.3383	2.9241	2.9613	2.8800	3.0000
8.2165	8.6021	7.7188	4.7494	4.9723	4.4617	2.9456	2.9799	2.9003	3.0000
8.4305	8.7995	7.8985	4.8732	5.0864	4.5656	2.9645	2.9968	2.9170	3.0000
8.5218	8.9011	7.9529	4.9259	5.1451	4.5971	2.9725	3.0055	2.9220	2.0000
8.5655	8.9409	7.9628	4.9512	5.1681	4.6028	2.9763	3.0088	2.9229	2.0000
8.5849	8.9719	7.9517	4.9624	5.1861	4.5964	2.9780	3.0114	2.9219	2.0000
8.5607	8.9770	7.8991	4.9484	5.1890	4.5660	2.9759	3.0118	2.9171	2.0000
8.4970	8.9137	7.8420	4.9116	5.1524	4.5329	2.9703	3.0065	2.9118	2.0000
8.4252	8.7864	7.8170	4.8700	5.0788	4.5185	2.9641	2.9957	2.9094	2.0000
8.3707	8.6628	7.8224	4.8385	5.0074	4.5216	2.9593	2.9851	2.9099	2.0000
8.3413	8.6393	7.8545	4.8216	4.9938	4.5402	2.9568	2.9831	2.9129	2.0000
8.3492	8.6511	7.9251	4.8261	5.0006	4.5810	2.9575	2.9841	2.9194	2.0000
8.4128	8.7146	8.0107	4.8629	5.0373	4.6305	2.9631	2.9896	2.9273	2.0000
8.5246	8.8171	8.1059	4.9275	5.0966	4.6855	2.9729	2.9983	2.9360	2.0000